

**LIQUID CRYSTAL TEMPLATED
SYNTHESIS OF METAL OXIDES
AND THEIR CHARACTERIZATION**

**A Thesis Submitted to
the Graduate School of
İzmir Institute of Technology
in Partial Fulfillment of the Requirements for the Degree of**

MASTER OF SCIENCE

in Chemistry

**by
SEREN DEMİR**

**December 2024
İZMİR**

We approve the thesis of **Seren DEMİR**

Examining Committee Members:

Asst. Prof. Dr. Fadime MERT BALCI
Department of Chemistry, İzmir Institute of Technology

Assoc. Prof. Dr. Nermin Seda KEHR
Department of Chemistry, İzmir Institute of Technology

Assoc. Prof. Dr. Muhammed ÜÇÜNCÜ
Department of Analytical Chemistry, İzmir Kâtip Çelebi University

5 December 2024

Asst. Prof. Dr. Fadime MERT BALCI
Supervisor, Department of Chemistry
İzmir Institute of Technology

Prof. Dr. Gülşah ŞANLI MOHAMED
Head of the Department of Chemistry

Prof. Dr. Mehtap EANES
Head of the Graduate School of
Engineering and Sciences

ACKNOWLEDGEMENTS

First of all, I would like to express my sincere gratitude to my advisor Assist. Prof. Dr. Fadime MERT BALCI, who guided me, supported me and sincerely motivated me in all kinds of negative situations and got me back on my feet throughout my undergraduate graduation project and Master's Thesis studies. I can never forget the beauties and information she gave me throughout my academic life.

I would like to thank the thesis committee members Assoc. Prof. Dr. Nermin Seda KEHR and Assoc. Prof. Dr. Muhammed ÜÇÜNCÜ for their valuable contributions to my studies and for accepting my thesis jury membership. I would like to thank Prof. Dr. Sinan BALCI, he always supported and encouraged me. I would also like to thank the IZTECH Materials Research Center, which ensured the completion of all my experimental studies, and all the lecturers there who contributed to my analyses for their patience and help.

And of course, I would like to thank my friends who are my dear sisters and my biggest sources of motivation, the dear friends that the university has given me, and all my other friends, colleagues, and lab mates who helped me pull myself together and smile when I lost my motivation.

And my greatest gratitude goes to my dear family, who are my greatest supporters in this life. I would like to express my gratitude to them for their endless trust in me, their endless encouragement, and their unwavering support, and I love them very much. If I could be the reason for the pride in their sparkling eyes looking at me and every smile on their faces, I would be very happy. And my dear niece PERA... you have been my greatest source of inspiration during this process. I hope that in the future, I can also be a scientist that you can inspire. I love you!

ABSTRACT

LIQUID CRYSTAL TEMPLATED SYNTHESIS OF METAL OXIDES AND THEIR CHARACTERIZATION

Liquid crystals are phases that exhibit properties between solids and liquids and have an important place in materials science and technology. These materials exhibit properties of both liquids and crystals due to their molecular arrangement and the freedom of movement of their molecules. In particular, thermotropic and lyotropic liquid crystals offer structures that can transition to different phases depending on temperature and solvent concentration. These transition processes increase the flexibility and functionality of liquid crystals, enabling their use in many areas from display technologies to biological applications. The mesophases of liquid crystals, such as nematic, smectic, and cholesteric phases, are categorized based on their molecular arrangement. In the nematic phase, molecules show a general orientation, while in the smectic phase, a layered order emerges. In the cholesteric phase, molecules form a spiral structure that gives rise to unique optical properties. These mesophases play a key role, especially in optoelectronic applications, sensors and biomimetic materials. Surfactants organize in the presence of water to form various lyotropic liquid crystal (LLC) mesophases. In this thesis, Molybdenum trioxide films were produced using Liquid Crystal mesophases and these films were characterized using different characterization techniques. In addition, Zinc oxide thin films were produced in the same way using liquid crystal templates and characterized using different characterization techniques. Furthermore, the effect of the positively charged CTAB surfactant on zinc oxide films was investigated. The band gap was calculated using a Tauc plot based on data from the absorbance graphs of zinc oxide films with varying thicknesses, which were measured using a profilometer. Additionally, ZIF-8, a metal-organic framework, was synthesized as a film using a 691 mM 2-HmIm solution and zinc oxide thin films.

ÖZET

SIVI KRİSTAL KALIPLAMALI METAL OKSİT SENTEZİ VE KARAKTERİZASYONU

Sıvı kristaller, katılar ve sıvılar arasında özellikler gösteren fazlar olup malzeme bilimi ve teknolojisinde önemli bir yere sahiptir. Bu malzemeler, moleküllerinin dizilimi ve hareket serbestliği sayesinde hem sıvıların hem de kristallerin özelliklerini birleştirir. Özellikle termotropik ve liyotropik sıvı kristaller, sıcaklık ve çözücü konsantrasyonuna bağlı olarak farklı fazlara geçiş yapabilen yapılar sunar. Bu geçiş süreçleri, sıvı kristallerin esnekliğini ve işlevselliğini artırarak, görüntüleme teknolojilerinden biyolojik uygulamalara kadar birçok alanda kullanılmalarını sağlar. Sıvı kristallerin sergilediği mezofazlar (örneğin nematik, smektik ve kolesterik fazlar) moleküler dizilimine göre sınıflandırılır. Nematik fazda moleküller genel bir yönelim gösterirken, smektik fazda katmanlı bir düzen ortaya çıkar. Kolesterik fazda moleküller spiral bir yapı oluşturarak optik özellikler gösterir. Bu mezofazlar, özellikle optoelektronik uygulamalarda, sensörlerde ve biyomimetik malzemelerde önemli rol oynar. Yüzey aktif maddeler, suyun varlığında çeşitli liyotropik sıvı kristal (LLC) mezofazları oluşturmak üzere organize olurlar. Bu tezde, Sıvı Kristal mezofazları kullanılarak Molibden trioksit filmleri sentezlendi ve bu filmler farklı karakterizasyon teknikleri kullanılarak karakterize edildi. Ayrıca, Sıvı Kristal şablonlu Çinko oksit ince filmler aynı şekilde sentezlendi ve farklı karakterizasyon teknikleri kullanılarak karakterize edildi. Ayrıca, Çinko Oksit filmler için pozitif yüklü CTAB yüzey aktif maddesinin filmler üzerindeki etkisi araştırıldı. Farklı kalınlıklardaki çinko oksit filmlerin absorbans grafiklerinden elde edilen veriler ve profilometre ile ölçülen kalınlıklar kullanılarak Tauc Plot ile bant aralığı hesaplaması yapıldı. Ayrıca, Metal Organik Çerçevelerden biri olan ZIF-8, Çinko oksit ince filmler üzerinde 691 mM 2-Hmlm çözeltisi kullanılarak sentezlendi ve karakterize edildi.

TABLE OF CONTENTS

LIST OF FIGURES	viii
CHAPTER 1. INTRODUCTION	1
1.1. Liquid Crystals	1
1.2. Lyotropic Liquid Crystalline Mesophases.....	4
1.3. Metal Oxides	6
1.4. Synthesis of Metal Oxides Using Lyotropic Liquid Crystals.....	8
1.5. Molybdenum Trioxide (MoO ₃)	11
1.6. Zinc Oxide (ZnO)	12
1.7. Zeolitic Imidazolate Framework (ZIF-8)	14
CHAPTER 2. MATERIALS & METHODS	16
2.1. Experimental Methodology	16
2.1.1. Synthesis of Molybdenum Oxide Films	16
2.1.2. Synthesis of Zinc Oxide and ZIF-8 Thin Films.....	17
2.2. Characterization Techniques	18
2.2.1. Polarized Optical Microscopy (POM)	18
2.2.2. UV-VIS Spectroscopy.....	18
2.2.3. Fluorescence Spectroscopy (FS5)	19
2.2.4. Scanning Electron Microscopy (SEM)	19
2.2.5. Energy-dispersive X-ray spectroscopy (EDS).....	19
2.2.6. X-Ray Diffraction (XRD).....	20
2.2.7. Raman Spectroscopy	20
2.2.8. AFM-Based Profilometer	21
CHAPTER 3. RESULTS & DISCUSSION	23
3.1. Synthesis and Characterization of Molybdenum Oxide Films Using Lyotropic Liquid Crystal	23
3.2. Synthesis and Characterization of Zinc Oxide Thin Films Using Lyotropic Liquid Crystal	28
3.3. Synthesis of Liquid Crystal Templated ZIF-8 Films	39

CHAPTER 4. CONCLUSION	42
REFERENCES	45

LIST OF FIGURES

<u>Figure</u>	<u>Page</u>
Figure 1.1. Liquid crystal. (Source: Yu, 2015) ¹	1
Figure 1.2. Liquid crystal pioneers. (a) Friedrich Richard Reinitzer (1857–1927) and (b) Otto Lehmann (1855–1922). (Source: DiLisi, 2019) ³	2
Figure 1.3. Types of Liquid Crystals. (Source: Rahman et al, 2020) ¹⁰	3
Figure 1.4. Schematic representation of the phase diagram of an amphiphilic surfactant in an isotropic solvent. (Source: Dierking I. and Al-Zangana S., 2017) ¹⁹	5
Figure 1.5. The four basic stages of spin coating. (Source: Maumen et al, 2021) ³¹	7
Figure 1.6. A scheme on the use of soft templating methods in the synthesis of mesoporous materials. (Source: Serra A., and Valles E.,2018) ⁷⁶	9
Figure 1.7. Two different crystal structures of molybdenum trioxide (a) α -MoO ₃ (orthorhombic) and (b) β -MoO ₃ (monoclinic). ⁷⁷	11
Figure 1.8. Wurtzite crystal structure of ZnO with a hexagonal unit cell and distinct crystal faces. ⁷⁸	13
Figure 1.9. Zeolitic Imidazolate Framework (ZIF-8). ⁷⁹	15
Figure 3.1 Photograph of the change of LC/AHM solution over time: (a) first minutes and (b) after 10 minutes.	23
Figure 3.2. SEM images of MoO ₃ films at different temperatures (a) Farthest and closest 250°C 3 hours (b) 350°C 2 hours (c) 450°C 1 hour.	24
Figure 3.3. EDS image of MoO ₃ film.	25
Figure 3.4. XRD pattern of SA/C ₁₂ EO ₁₀ and SA/C ₁₂ EO ₁₀ /AHM LLC mesophases.	25
Figure 3.5. XRD pattern at different temperatures.	26
Figure 3.6. Photograph of films calcined at different temperatures on a glass slide. The temperatures are (a) 250°C (b) 350°C and (c) 450°C, respectively.....	27
Figure 3.7. Raman Peaks at different temperatures for orthorhombic a-MoO ₃ films. ...	28
Figure 3.8. Photographs of solutions with CTAB (2C) and without CTAB (2) with a mole ratio of 2.	29
Figure 3.9. (a) Low angle XRD pattern (b) POM image of Zn/LC.	29

<u>Figure</u>	<u>Page</u>
Figure 3.10. The XRD graphs of ZnO films calcined at different temperatures (a) without CTAB, and (b) with CTAB.	30
Figure 3.11. SEM images ZnO thin films at different temperatures (a) 250°C (b) 350°C (c) 450°C with CTAB and (d) 250°C (e) 350°C (f) 450°C without CTAB.	31
Figure 3.12. Full-area EDS analysis of the glass substrate.....	32
Figure 3.13. EDS mapping for ZnO thin film.....	33
Figure 3.14. Emission mapping for ZnO thin film.	34
Figure 3.15. Profilometer images showing the thickness of Zinc Oxide thin films at different spin-coating speeds: (a) 500 rpm (b) 1000 rpm and (c) 2000 rpm.	35
Figure 3.16. Photoluminescence (PL) spectra of ZnO films produced at different spin-coating speeds (500, 1000 and 2000 rpm): (a) without CTAB (b) with CTAB.	36
Figure 3.17. Absorbance spectra of ZnO films fabricated at different spin-coating speeds (500, 1000 and 2000 rpm): (a) without CTAB (b) with CTAB.....	37
Figure 3.18. Eg determination of ZnO films different thicknesses; (a) 500 rpm, (b) 1000 rpm, (c) 2000 rpm.	38
Figure 3.19. ZnO Thin Film(a) ZIF-8 Film(b).....	39
Figure 3.20. XRD graphs of ZIF-8 film structures synthesized by applying different temperature/time parameters.	40
Figure 3.21. SEM images of ZIF-8 film structures formed from Zinc Oxide thin films by applying different temperature/time parameters: (a) 30°C 3 hours, (b) 30°C 6 hours, (c) 60°C 3 hours and (d) 60°C 6 hours.....	41

CHAPTER 1

INTRODUCTION

1.1. Liquid Crystals

These days, LC displays (LCDs) are widely known. But LCDs and liquid crystals (LC) are not quite the same. After the first three states, liquid crystals are generally regarded as the fourth state of matter. Because they possess both the orderliness of a crystalline solid and the controllable mobility of a liquid, LCs are regarded as the intermediate phase of matter.¹

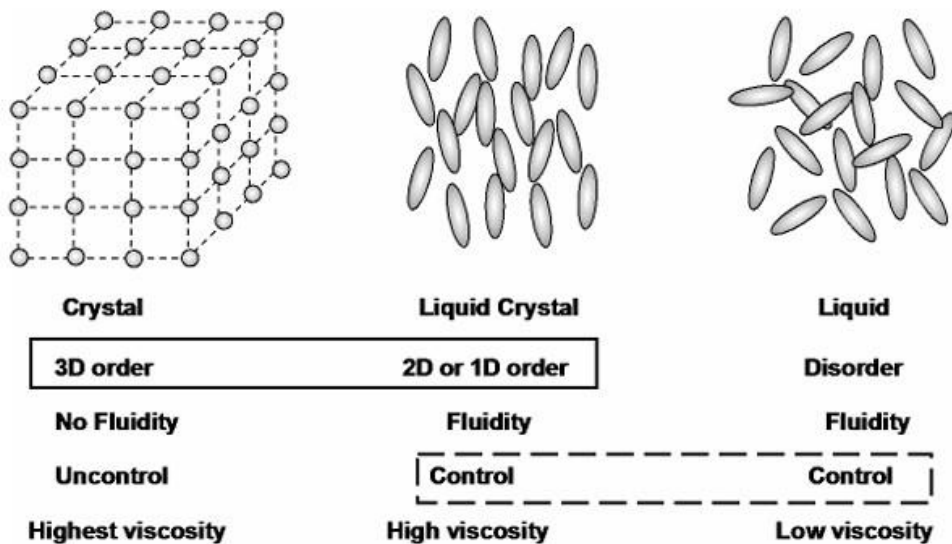


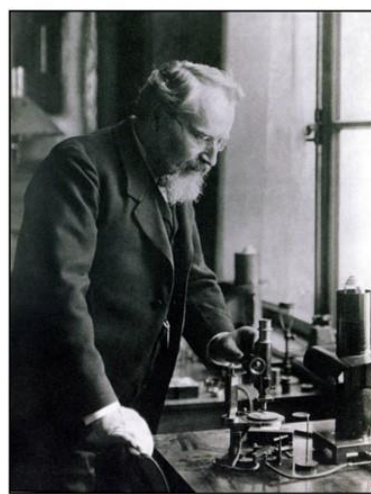
Figure 1.1. Liquid crystal. (Source: Yu, 2015)¹

Crystal structures are difficult to control due to their lack of fluidity, while the fluidity of liquids can be controlled. As shown in Figure 1.1. Liquid crystal, liquid crystals are a fluid phase and have high viscosity, so their controllability is higher than the crystal structure.²

The discovery of Liquid Crystals began in the late 19th century with Austrian botanist and chemist Friedrich Reinitzer Figure 1.2(b). While studying cholesterol from carrots, Reinitzer noticed that cholesteryl benzoate had two melting points associated with 'birefringence' and colour changes. Cholesteryl benzoate, despite its optical properties being similar to those of crystals, still flowed like a liquid. In 1888, Reinitzer wrote a letter to German physicist Otto Lehmann Figure 1.2(a) stating that the substance he had studied appeared cloudy and liquid-like at 145.5 °C, and became completely clear at 178.5 °C.³



(a)



(b)

Figure 1.2. Liquid crystal pioneers. (a) Friedrich Richard Reinitzer (1857–1927) and (b) Otto Lehmann (1855–1922). (Source: DiLisi, 2019)³

Liquid crystals are usually divided into two groups thermotropic and lyotropic phases. Thermotropic liquid crystals are sensitive to temperature changes and undergo a transition to the liquid crystal phase with each increase in temperature. Lyotropic liquid crystals, on the other hand, undergo phase transitions influenced by both temperature and the concentration of molecules, with water being the common solvent in this type.⁴ Although these two types of liquid crystals have almost similar physical and chemical properties, the chemical structures of their molecules are quite different.

Thermotropic liquid crystals⁵ change to liquid crystal form depending on the temperature. As a result, raising and lowering the temperature of a substance is an approach that supports the formation of thermotropic liquid crystals. In contrast, the formation of lyotropic liquid crystals depends on surfactant concentration and temperature.⁶⁻⁸ In other words, lyotropic liquid crystals will form in both lyophilic (solvent-attracting) and lyophobic (solvent-repelling) environments.⁹

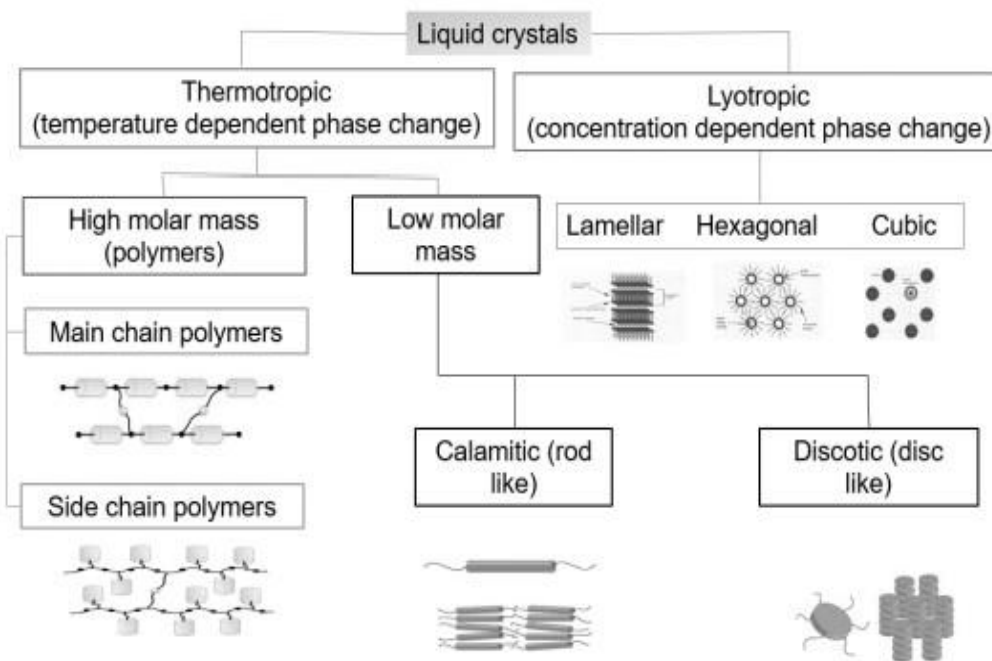


Figure 1.3. Types of Liquid Crystals. (Source: Rahman et al, 2020)¹⁰

It is also visualized as a schema in Figure 1.3. In general, liquid crystals are classified into two types: phases that vary with temperature and phases that vary with concentration. The optical properties of thermotropic and lyotropic liquid crystals vary during phase transitions due to their regular molecular structures. Thermotropic liquid crystals undergo transitions into different optical phases as a result of temperature changes. In these phases, they exhibit properties such as changing the polarization of light. Lyotropic liquid crystals form regular structures that change with solvent concentration and temperature; their optical properties are generally associated with micellization and the development of liquid-crystal order. Both types of liquid crystals exhibit different color and textural properties when observed under polarized light, which are used to identify their phase states.¹¹ Liquid crystals have a wide range of applications,

especially in optics and electronics.¹² The ability of LCs to change light polarization with the help of electric fields, their structures resistant to different environmental conditions and their ability to change light/color properties are interesting for various application areas. For this reason, Liquid Crystals are often preferred for use in display technologies and sensor applications.¹³

1.2. Lyotropic Liquid Crystalline Mesophases

The lyotropic liquid crystal mesophases are systems in which amphiphilic molecules form ordered structures capable of undergoing phases in response to changes in concentration.¹⁴⁻¹⁶ These kinds of liquid crystals form by dissolving amphiphilic molecules in a solvent (usually water)¹⁷ and display characteristics of both liquids and solids, forming ordered formations at specific concentrations. Amphiphilic substances are those that contain both hydrophilic and hydrophobic ends. Micelle-like structures will arise as a result of these molecules' self-organization into mesophases upon entering the solvent. These liquid crystal mesophases can transition from one phase to another depending on environmental factors such as concentration and temperature.¹⁸

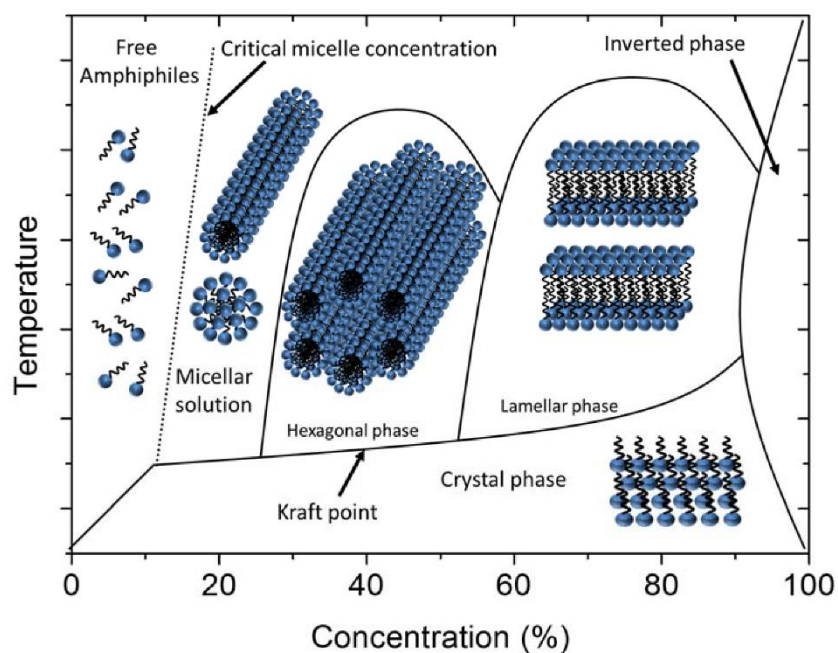


Figure 1.4. Schematic representation of the phase diagram of an amphiphilic surfactant in an isotropic solvent. (Source: Dierking I. and Al-Zangana S., 2017)¹⁹

The formation of micelles results in regular structures that change depending on physical parameters such as temperature and concentration. The phase diagram above Figure 1.4 shows how amphiphilic molecules (one end is hydrophilic, the other end is oil-loving) are arranged at certain temperatures and concentrations. At low concentrations, the molecules are dispersed in solution as free amphiphiles, while when the critical micelle concentration (CMC) is exceeded, spherical structures called micelles are formed. The formation of these structures is associated with the amphiphiles transitioning to a more energetically stable state.

With increasing concentration and appropriate temperature levels micelles transform into more complex structures. In this process, regular liquid crystal phases such as hexagonal, lamellar and reversed phases are observed, respectively. The hexagonal phase consists of regular arrangements of cylindrical structures, while the lamellar phase consists of double-layer structures. At higher concentrations, liquid crystal phases have dense arrangements. This entire process depends on the molecular structure of the amphiphilic molecules and the environmental conditions, and reflects the dynamic and versatile properties of liquid crystals.

Micelles are spherical, self-assembled structures in which the polar head groups of amphiphiles form a hydrophilic shell that encloses their apolar tail groups.²⁰ For

instance, as the concentration of amphiphiles rises, a system that is in a micellar phase at low concentrations can change into lamellar, hexagonal, or cubic phases. The cubic phase has a highly intricate three-dimensional structure, the hexagonal phase is made up of cylindrical formations, and the lamellar phase has an organized structure where molecules form parallel sheets. The arrangement of the molecules in the solvent varies across phases.

To summarize briefly, below the critical micelle concentration (cmc), amphiphilic molecules diffuse freely in the solvent, while above this value they can form spherical, disk or rod-like structures. As the concentration increases further, these micelles aggregate to form ordered structures such as hexagonal, cubic or lamellar phases. These phase diagrams are quite complex because they are sensitive to temperature and concentration.²¹

1.3. Metal Oxides

Metal oxides are inorganic compounds that form when metals react with oxygen. Generally, these substances are highly stable. Depending on the kind of metal and how it bonds with oxygen, metal oxides have different structures. Ionic bond-formed metal oxides typically consist of alkali and alkaline earth metal oxides and possess characteristics like electrical conductivity and elevated melting temperatures. However, the oxides of transition metals and certain semimetals are known to contain metals with covalent connections.

Today, metal oxides play a critical role in various areas from industry to electronics. For example, the electrochemical properties of molybdenum oxide (MoO_3)²² allow it to be used as an anode material in batteries and supercapacitors, while MoO_3 is also used as a transparent conductive layer in thin-film semiconductors.²³ While zinc oxide (ZnO) is more suitable for use in gas sensor materials²⁴ in thin film form due to its tunable structure and wide optical band gap, metal oxides such as titanium dioxide (TiO_2) are commonly used in paints and sunscreens. In addition, metal oxides such as iron oxide (FeO) are widely used in the production of pigments²⁵ and magnets. They also play an important role as electrode materials in energy storage systems,²⁶ especially batteries and fuel cells.²⁷ Since PEC (photoelectrochemical)²⁸ water splitting is increasing, titanium oxides and iron oxides are also of great importance in light-driven photocatalysis studies.

The chemical reactivity and thermal stability of these compounds make them indispensable in environmental protection, catalyst development and high-tech devices.

In literature studies, metal oxides are synthesized using various methods. For example, an aerosol-chemical vapor deposition (ACVD)²⁹ method has been used for the controlled deposition of nanostructured metal oxide films. In this method, different characteristic times and parameters that enable the deposition of the film were evaluated to understand their effect on the morphology of the film. Another method of metal oxide synthesis, the sol-gel method,³⁰ is based on the principle that the system which starts as a sol (solution) gradually transforms into a gel-like network (gel) structure containing both liquid and solid phases. Generally, sol formation occurs through the hydrolysis and condensation of metal alkoxide precursors.

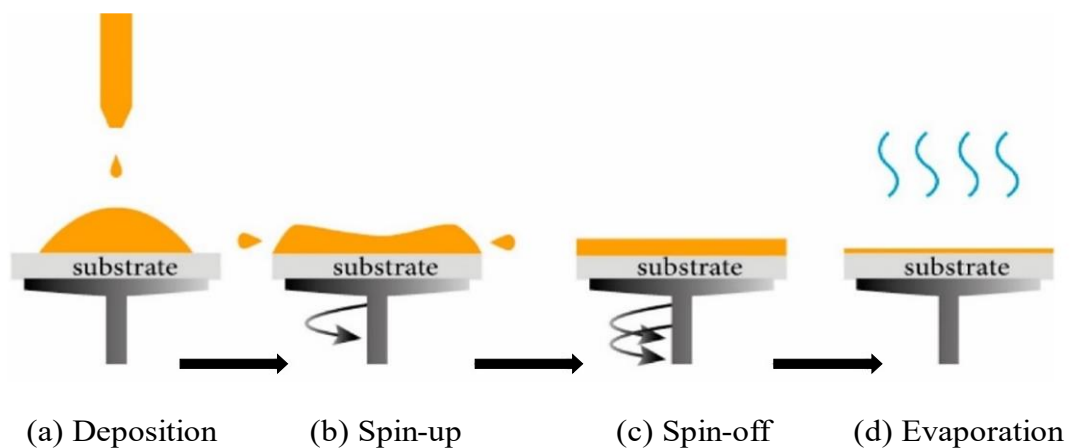


Figure 1.5. The four basic stages of spin coating. (Source: Maumen et al, 2021)³¹

Finally, the Spin Coater is based on the principle of spreading a metal oxide solution onto a substrate by rotation to provide a homogeneous coating. The process consists of four main steps as seen in Figure 1.5: Deposition (a): The substrate is covered with a drop of metal oxide solution. A metal precursor (such as metal nitrates or organometallic compounds) and a solvent are typically included in this solution. Spin-up (b): High-speed rotation of the substrate is initiated. At this stage, the surplus solution in the middle of the substrate flows outward. The uniform distribution of the solution throughout the surface is ensured by centrifugal force. Spin-off (c): By using faster rotation speeds, extra solution is eliminated from the surface. This procedure guarantees the creation of a thin, consistent film layer. The coating thickness can be altered by

varying the spin speed and viscosity of the solution. Evaporation (d): The gel film layer is left behind after the solvent evaporates during the coating process. Usually, a heat treatment (such as drying or pyrolysis) is applied to ensure that the metal forms. The Spin Coater method is preferred in thin film technologies because it provides precise and reproducible coatings. In metal oxide syntheses, this method is quite common to produce nanostructured and homogeneous films. This process ensures that the material is distributed evenly and uniformly across the entire substrate surface.³²

1.4. Synthesis of Metal Oxides Using Lyotropic Liquid Crystals

Metal oxides are widely used inorganic compounds formed by the combination of metal elements with oxygen. To improve various electro-optic and other important properties of Liquid Crystals, many studies have been conducted on the incorporation of appropriate additives into the host Liquid Crystal material.³³ Porous crystalline metal oxide semiconductor films³⁴ have led to numerous applications such as optoelectronic devices, solar cells, chemical sensors, and photocatalysis.³⁵

From the past to the present, soft templates containing surfactants that encourage pore development have been used to create metals, metal oxides, and polymers. The final solid material's morphology adopts the structure of soft systems with nanoscale motion dynamics as a result of the reaction of inorganic precursors in a non-homogeneous surfactant. Compared to the hard templating approach, it requires fewer synthetic procedures, is less expensive, and allows for control over pore size and mesostructure by regulating the dynamic structure of the chosen soft system.³⁶

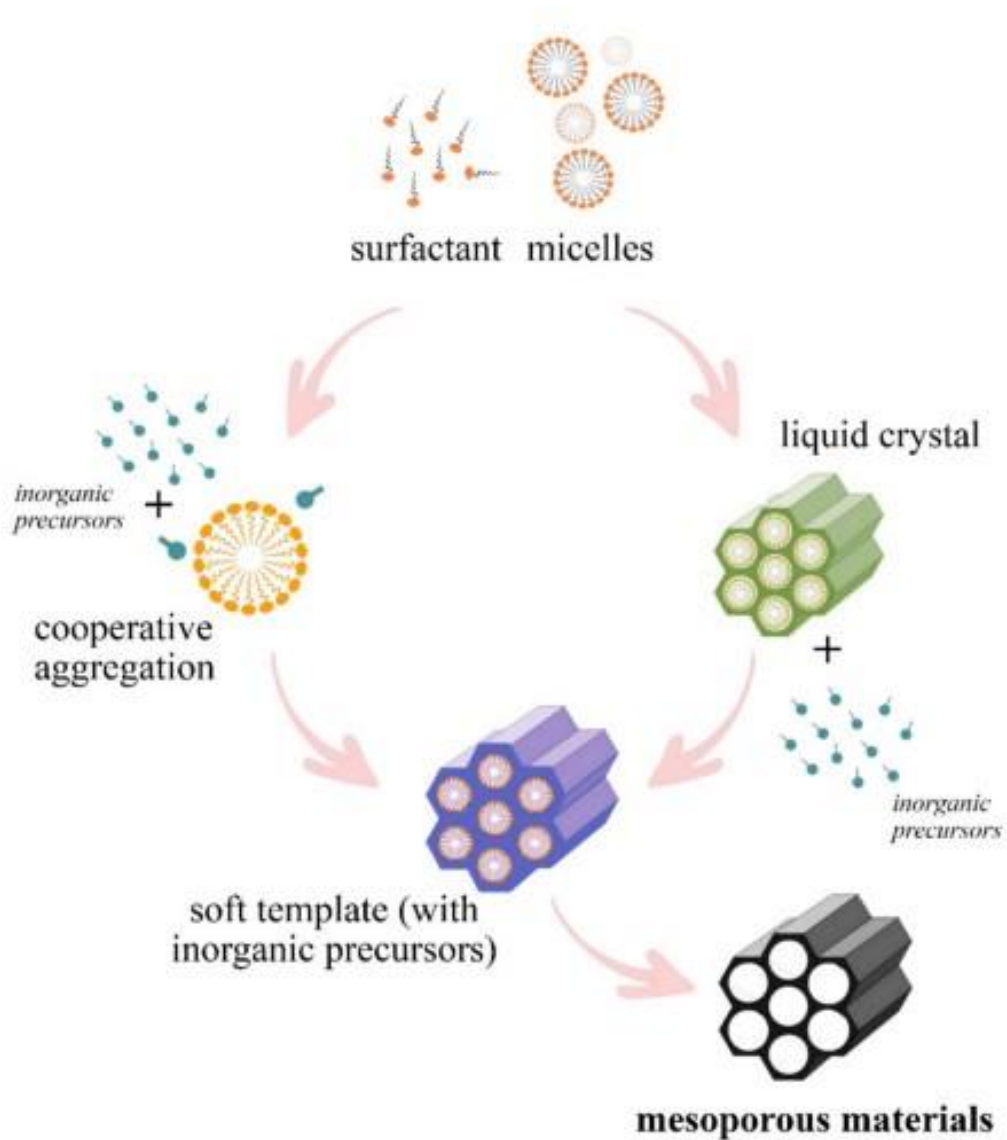


Figure 1.6. A scheme on the use of soft templating methods in the synthesis of mesoporous materials. (Source: Serra A., and Valles E.,2018)⁷⁶

The liquid crystal templating method's steps are shown in Figure 1.6, which also illustrates the fundamental procedure for creating mesoporous (porous) materials. Surfactants create spherical structures known as micelles in the first step by self-assembling in a solvent. These micelles arise because of the hydrophilic (it attracts water) and hydrophobic (it repels water) properties of the surfactant. Surfactants are templates that form regular structures.

In the second step, inorganic precursors are added to these micelles formed by the surfactants. Inorganic substances accumulate in an orderly manner around the micelles and are called aggregation. In a process known as aggregation, inorganic materials and surfactants come together to form organized structures. The liquid crystals make up the fundamental structure of mesoporous materials and have an ordered structure. The inorganic precursors then condense around the surfactant template to form a "soft template". This template is essential to the development of mesoporous materials' porous structure. Surfactants are typically eliminated or separated at the end of the process, leaving just the inorganic mesoporous substance. The result is a mesoporous material with a high surface area, a well-defined and controlled pore structure, and properties suitable for various applications. The synthesis of mesoporous materials, which are crucial for numerous applications like energy storage devices, drug delivery systems, sensors, and catalysts, is frequently accomplished using this technique. An efficient way to regulate the pore arrangement and size of these materials is using liquid crystal phases and surfactant-based procedures.

The relatively rich liquid crystal phase of lyotropic liquid crystals is a complex system composed of surfactants and solvents. Because of the ordered phases that the surfactant forms, these structures serve as a soft template that enables the directed and controlled production of mesoporous nanomaterials. The advantages of lyotropic liquid crystals, such as their strong versatility, ease of control and adaptability, make them more efficient, economical and practical compared to traditional hard template methods.³⁷ In addition, this method attracts attention with its potential to support environmentally friendly processes. One particularly effective method for creating various nanopore geometries and facilitating the creation of materials with a high pore density is the use of lyotropic liquid crystal templates. These templates' capacity to offer exact control at the nanoscale has led to creative solutions in the fields of materials science and nanotechnology. Thanks to the design of their pore architectures, the resulting materials have found a wide range of applications and have garnered attention, particularly in fields like energy storage systems, catalysts, and sensors. Thus, they make significant contributions to research in this field by inspiring the development of new approaches in nanomaterial production.³⁸

1.5. Molybdenum Trioxide (MoO₃)

When molybdenum and oxygen react, a metal oxide called molybdenum oxide is formed, which is typically white or pale yellow in color. Although this molecule can exist in a variety of oxidation states, the most typically employed form is molybdenum trioxide (MoO₃). When exposed to UV light, its hue changes from white-yellow to greenish blue due to its different features, which include electrochromic³⁹ and photochromic behavior.⁴⁰ This material is classified as an n-type semiconductor because of its electron transport characteristics. It can become more electrically conductive⁴¹ as oxygen vacancies form on its surface. The typical interaction of molybdenum metal and oxygen yields molybdenum oxide, which can be obtained through thermal oxidation at high temperatures.

Alternatively, other synthesis techniques, such as sol-gel,⁴² hydrothermal processes,⁴³ thermal evaporation,⁴⁴ or chemical vapor deposition,⁴⁵ can also be employed to produce MoO₃ with varying properties and morphologies. The most stable and commonly encountered form of MoO₃ is the α -MoO₃ phase, which is characterized by an orthorhombic crystal structure. This phase is widely studied due to its robust thermal and structural stability.

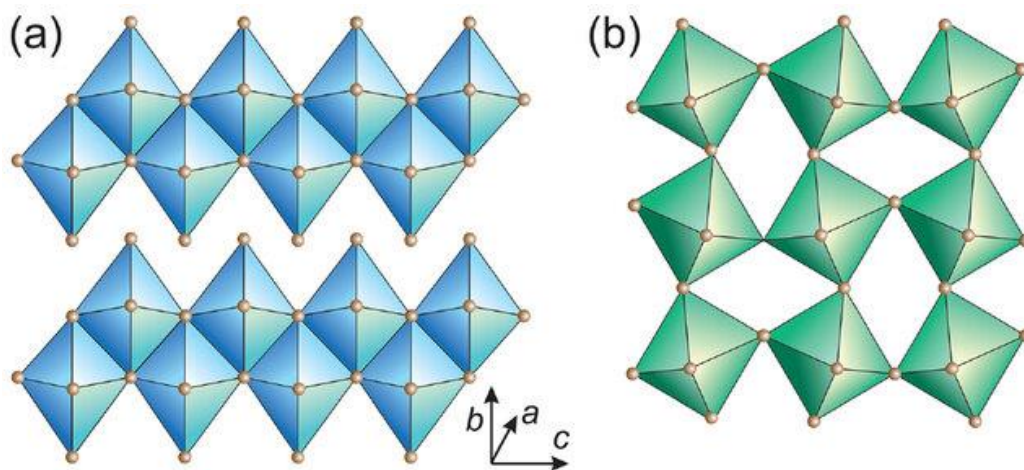


Figure 1.7. Two different crystal structures of molybdenum trioxide (a) α -MoO₃ (orthorhombic) and (b) β -MoO₃ (monoclinic).⁷⁷

The Figure 1.7 above shows two different phases of molybdenum trioxide (MoO_3) crystals, α - MoO_3 and β - MoO_3 . Figure (a) represents the orthorhombic crystal structure of α - MoO_3 . This phase consists of distorted octahedral units formed by Mo atoms and oxygen atoms, and these octahedra are organized into a chain. The structure is arranged in layers connected to each other in different planes, which causes α - MoO_3 to exhibit sheet-like properties. Figure (b) represents the monoclinic crystal structure of β - MoO_3 . This phase has a more tightly packed structure and shows that the octahedral MoO_6 units are arranged more densely in a different order. This structure exhibits less anisotropic properties compared to the α phase. Both structures have different physical and chemical properties and are used in catalysis, gas sensors and energy storage applications. In addition to α - MoO_3 , less stable forms such as the β - MoO_3 phase, characterized by a monoclinic crystal structure, and amorphous molybdenum oxide also exist. These different phases arise from variations in synthesis conditions and exhibit distinct thermal,⁴⁶ optical,⁴⁷ and electronic properties due to their unique crystal arrangements.

In summary, Molybdenum trioxide (MoO_3), especially with its α - and β -phases, has attracted attention as an important material for energy storage⁴⁸ and electronic applications. α - MoO_3 generally starts to nucleate at approximately 300 °C. On the other hand, the evaluation of β - MoO_3 as a cathode material in thin-film lithium-ion batteries⁴⁹ emphasizes the importance of long-term annealing to increase the crystallinity⁵⁰ and improve the performance of thin-film electrodes.⁵¹ Interestingly, β - MoO_3 crystals transition to a similar lithiated electrochemical state as α - MoO_3 during cycling. Both phases can be crystallized at relatively low temperatures, allowing MoO_3 to be investigated as a versatile material in various technological applications.

1.6. Zinc Oxide (ZnO)

In recent years, Zinc oxide (ZnO) has become one of the most extensively studied semiconductor metal oxides for various applications, thanks to its diverse characteristics, including non-toxicity, simple synthesis, adjustable wide direct band gap (~ 3.4 eV),⁵² high exciton binding energy (~ 60 meV), and excellent transparency in the visible spectrum.⁵³ Zinc Oxide exists in two different crystal structures: hexagonal wurtzite and cubic zinc blende. The wurtzite structure is the more stable form under normal conditions and allows for effective growth of ZnO when conditions are optimum.⁵⁴

The optical, electrical, and surface characteristics of zinc oxide (ZnO) films are largely determined by their crystal structure, which also influences how ZnO behaves in different applications. The tetrahedral coordination of both zinc and oxygen atoms is a characteristic of the wurtzite crystal structure that ZnO typically takes on. The zinc and oxygen atoms are organized in a distinct, regular manner⁵⁵ in this specific configuration, which produces a crystal lattice with hexagonal symmetry. In addition to being the most prevalent form of ZnO in nature, the wurtzite structure is the most stable configuration under normal circumstances, providing it with special qualities that are useful in a range of technological applications.

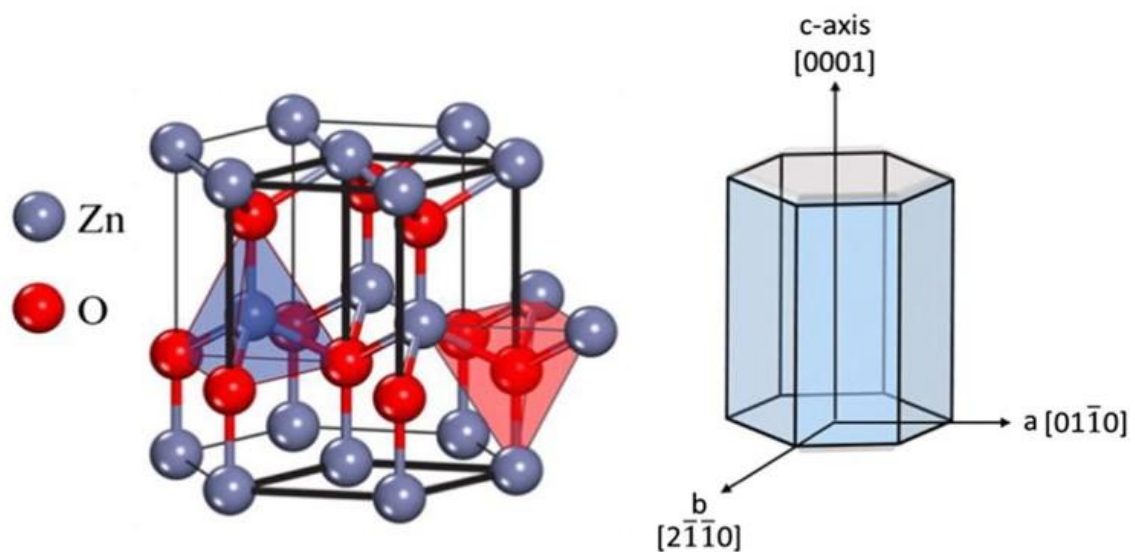


Figure 1.8. Wurtzite crystal structure of ZnO with a hexagonal unit cell and distinct crystal faces.⁷⁸

The Figure 1.8 shows a special structure called wurtzite in a zinc oxide (ZnO) crystal. The left image details the atomic-scale arrangement of Zn and O atoms. In this case, the red spheres represent oxygen (O) atoms, while the blue spheres represent zinc (Zn) atoms. Each zinc atom is connected to four oxygen atoms, and each oxygen atom is bonded to four zinc atoms, forming a tetrahedral structure. This configuration contributes to ZnO's piezoelectric and optical characteristics by forming a stiff three-dimensional lattice structure. The wurtzite structure's general geometric model is shown in the image on the right. A hexagonal prism-shaped crystal lattice is shown in this model. An essential part of ZnO's piezoelectric properties is the vertically oriented c-axis ([0001]), which shows the structure's polar direction. The hexagonal symmetry is defined by the

horizontal plane's a and b axes. This hexagonal arrangement makes ZnO preferred in many fields such as sensors, nanotechnology and optoelectronic devices. This regular atomic arrangement in the wurtzite crystal structure forms a foundation that enhances the strength and electrical properties of ZnO.

In short, Zinc oxide (ZnO) thin films are of great importance for many technological applications and can be produced by different synthesis methods. The sol-gel method⁵⁶ attracts attention with its low cost, easy applicability and ability to deposit homogeneous films on large areas. This method generally involves preparing solutions of metal nitrates and applying these solutions to the coating surface at a certain temperature.⁵⁷ Subsequently, organic components are removed by thermal treatment and the formation of the crystal structure of ZnO is ensured. The sol-gel method⁵⁸ is especially suitable for use in thin film optoelectronic devices.⁵⁹

1.7. Zeolitic Imidazolate Framework (ZIF-8)

Metal-organic frameworks (MOF) are porous materials formed by the combination of metal ions or metal clusters and organic binders.⁶⁰ Figure 1.9 shows the crystal structure of the ZIF-8 structure. ZIF-8 is formed by the coordination of zinc (Zn) metal atoms with imidazolate ($C_3H_3N_2^-$) ligands. In the image, the blue tetrahedra represent the four-coordination geometry of zinc atoms with imidazolate groups, while the orange and brown atoms represent carbon (C) and nitrogen (N) atoms, respectively. This structure forms a regular three-dimensional porous framework similar to zeolites. The most important properties of ZIF-8 include its high thermal and chemical stability, hydrophobic nature and very high porosity.

Because of their high surface area, chemical characteristics, and tunable pore size, these materials can be employed in a variety of applications, including drug delivery, membrane technologies,⁶³ energy and gas storage,⁶² separation, catalysis,⁶⁴ and batteries.⁶¹ ZIF-8, a member of the MOF family, is composed of zinc ions coordinated with an organic 2-methylimidazole ligand.

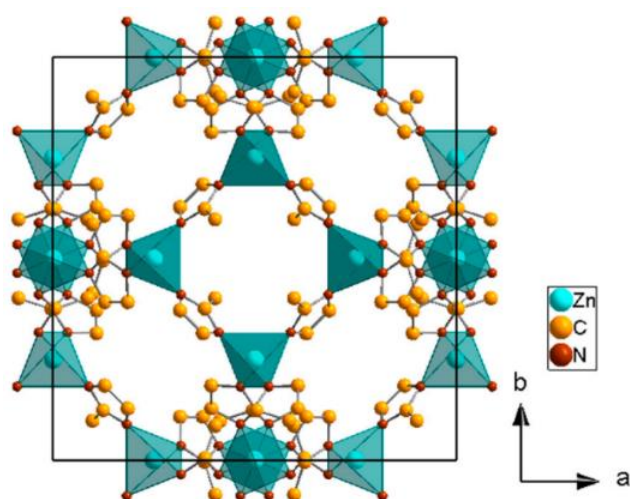


Figure 1.9. Zeolitic Imidazolate Framework (ZIF-8).⁷⁹

ZIF-8 films can be tailored to desired properties through various synthesis methods, highlighting their flexibility and adaptability. The first synthesis methods, the Dip Coating method,⁶⁵ creates a homogeneous film layer on the surface by dipping the substrate into the ZIF-8 precursor solution and slowly removing it, and this method is especially suitable for producing thin films. Chemical vapor deposition (CVD) is used in the production of sensitive and porous films by evaporating metal and organic components and depositing them on a surface.⁶⁶ Drop casting is another method used to synthesize ZIF-8 films. In this method, the metal ions of ZIF-8 and the organic ligand solution (usually 2-methylimidazole) are combined and the resulting precursor solution is directly dropped onto a substrate surface.⁶⁷

The solution spreads over the substrate and the ZIF-8 layer gradually begins to form as the solvent evaporates. The thickness and uniformity of the resulting film can be controlled by the amount, concentration and evaporation rate of the dropped solution. Spin Coating allows the precursor solution to be poured onto a surface and spread homogeneously by spinning, and is generally preferred in membrane applications.⁶⁸ In addition, the electrochemical deposition method offers the advantage of controlling the film thickness and order by depositing metal ions on an electrode. These methods offer the opportunity to optimize film properties for applications such as gas separation,⁶⁹ catalysis or water treatment.

CHAPTER 2

MATERIALS & METHODS

2.1. Experimental Methodology

2.1.1. Synthesis of Molybdenum Oxide Films

Ammoniumheptamolybdate tetrahydrate ($(\text{NH}_4)_6\text{Mo}_7\text{O}_{24}\cdot 4\text{H}_2\text{O}$) (abbreviated as AHM), decaethylene glycol monododecyl ether (10-lauryl ether, $\text{C}_{12}\text{E}_{10}$), and Sulfuric acid (SA or H_2SO_4 , 95–97%) were used in the production of molybdenum oxide films. All glass substrates and silicon wafers were cleaned with piranha solution ($\text{H}_2\text{SO}_4/\text{H}_2\text{O}_2$, 3:1 by volume) followed by sequential washing with alcohol and Milli-Q water prior to use. Milli-Q water (18.2 M Ω -cm resistivity at 25 °C) was used throughout the synthesis.

First, an SA/LC solution with a molar ratio of 2.5 was prepared. A clear liquid crystal solution was obtained by dissolving 627 mg of oligo (10-lauryl ether, $\text{C}_{12}\text{E}_{10}$) in 3 mL of ultrapure water in a glass bottle while stirring at 300 rpm, followed by the addition of 138 μL of sulfuric acid. Then, a clear AHM solution was prepared by dissolving 1.85 g of ammonium heptamolybdate tetrahydrate in 3 mL of ultrapure water to achieve a concentration of 0.5 M, in a separate Falcon tube. It was determined that 400 μL of the 0.5 M AHM solution is the optimal volume to be added to the 2.5 SA/LC solution. The reason for taking 400 microliters of the prepared AHM solution is that it was added in a controlled manner so that the liquid crystal phase would not be disrupted by including every 100 microliters into the system and the phase was disrupted after 400 microliters.

Since the obtained yellow transparent solution darkened and lost its transparency in approximately 10 minutes, the coating time was kept short and the coating of silicon wafer and glass surfaces was carried out by spin coating method at 1000 rpm for 1 minute. In order to obtain a thin film after spin coating, the coated films were calcined at different temperature parameters (450°C for 1 hour, 350°C for 2 hours and 250°C for 3 hours) to remove liquid crystal and carbon from the coated films and thus a film supporting metal oxide synthesis was formed.

2.1.2. Synthesis of Zinc Oxide and ZIF-8 Thin Films

The chemicals used in the synthesis of zinc oxide thin films were, zinc nitrate hexahydrate ($\text{N}_2\text{O}_6\text{Zn}\cdot 6\text{H}_2\text{O}$), decaethylene glycol monododecyl ether (10-lauryl ether, $\text{C}_{12}\text{E}_{10}$) and hexadecyltrimethylammonium bromide ($\text{CTAB} \geq 99\%$ purity). All glassware was cleaned with piranha solution and Milli-Q ($18.2 \text{ M}\Omega\text{-cm}$ resistivity at 25°C) water was used throughout the synthesis.

The Zinc Salt/ $\text{C}_{12}\text{EO}_{10}$ molar ratio used in the synthesis of liquid crystal-templated zinc oxide thin films was 2. In the synthesis, 4 mL of ethanol and 1 mL of ultrapure water were mixed in a glass bottle, then 0.500 g of nonionic surfactant (10-lauryl ether, $\text{C}_{12}\text{E}_{10}$) was added to the bottle and mixed homogeneously using a magnetic stirrer at 200 rpm. 0.442 g of zinc salt, corresponding to a 2 molar ratio, was added to the prepared surfactant solutions. The entire solution was stirred in the same manner with a magnetic stirrer at 200 rpm, resulting in a transparent, clear solution. Furthermore, CTAB, a positively charged surfactant, was added to the system to assess its effect on film quality. For Zn/LLC solutions with a mole ratio of 2, 0.145 g of CTAB was added to the system, achieving a molar ratio of 0.5 CTAB/ $\text{C}_{12}\text{EO}_{10}$. The obtained LLC solutions with and without CTAB were poured dropwise onto the glass substrate for XRD analysis and coated by spin coating method at 500 rpm for 2 minutes. For SEM analysis, the LLC solution was poured onto the glass substrate and coated by spin coating method at 2000 rpm for 2 min. Calcination was performed in an oxygenated environment at 250°C for 5 hours, 350°C for 3 hours, and 450°C for 1 hour to remove the liquid crystal and synthesize zinc oxide.

ZnO thin films obtained through the liquid crystal templated approach were treated with a 691 mM 2-methylimidazole solution to form ZIF-8 films. The oven parameters for the production of ZIF-8 films were 30°C for three hours, 30°C for six hours, 60°C for three hours, and 60°C for six hours. Following heat treatment, the films were removed from the solution container and rinsed with water. The resulting ZIF-8 film was then allowed to dry at ambient temperature.

2.2. Characterization Techniques

2.2.1. Polarized Optical Microscopy (POM)

Polarized waves cannot pass through the second filter, which is positioned perpendicular to the first filter. The light is split into two distinct components by the presence of birefringent samples in the light path, which causes the components to refract in different directions. This procedure produces an observable texture as the light whose polarization is altered by the sample goes through the second filter. POM exhibits birefringence, which is one of the key characteristics that distinguish liquid crystals. The different colors and patterns observed with POM result from changes in the polarization of light caused by the structure of liquid crystals. A black image is produced when a sample without birefringence is used, as light cannot pass through the analyzer. Molecular regularity causes the polarization state of light to shift when the liquid crystal sample is placed in the light path, altering the light's polarization state.⁷⁰ In POM, this shift is manifested as various hues and designs. The liquid crystal's phase state, molecular orientation, and thickness all affect the colors and patterns.

2.2.2. UV-VIS Spectroscopy

UV-VIS spectroscopy is a type of analysis that measures the amount of light absorbed by a substance. Through the use of visible and ultraviolet light spectra, this method offers details about the composition of the material. First, specific wavelengths of light are directed at the sample to begin this analysis. The sample's structure determines its ability to partially absorb or transmit certain wavelengths of light. This procedure measures the amount of light that the sample absorbs, allowing for the examination of its constituent parts. The process of UV-Vis analysis involves sending light from a light source to the sample and using a detector to measure the light's passage through the sample. The wavelengths of light that the substance absorbs are noted by the detector. An absorption spectrum is subsequently produced by converting the collected data into a signal. Numerous details regarding the sample's concentration and composition are revealed by this spectrum.

2.2.3. Fluorescence Spectroscopy (FS5)

Fluorescence is a form of photoluminescence in which a substance absorbs light and subsequently releases the energy as light. The energy received during the excitation of a fluorescent material raises the energy level of the substance's electrons. When the electrons return to the closest excited electronic level without losing energy, no light is released. As the excited electrons try to return to their ground energy level, they release their excess energy as photons. This kind of light emission is thought to be the fluorescent material's characteristic light. A monochromator or filter is used to select the wavelength of light that the light source produces, which is then directed towards the sample in a fluorescence measurement. The fluorescent light of a particular wavelength is isolated and measured using a second monochromator or filter because the photons released from the sample are dispersed in all directions. The detector is positioned perpendicular to the light source in order to stop the excitation light from being transmitted. This setup ensures that only the fluorescent light emitted by the sample is detected and analyzed. This procedure provides a reliable measurement to understand the sample's chemical and structural characteristics.

2.2.4. Scanning Electron Microscopy (SEM)

A material imaging method called scanning electron microscopy is used to assess a sample's surface thickness, appearance, and roughness. High-energy electrons are applied to the sample's surface during this analysis, and the surface is scanned to examine the material's appearance. The interaction of electrons with the sample's atoms yields comprehensive information about the sample's surface. The SEM instrument can be used for elemental analysis by examining the X-rays emitted from the sample. Because of this property, the SEM can photograph the surface's structure and shape while also analyzing its chemical composition. This technology's capacity to produce high-resolution images is crucial for materials science.

2.2.5. Energy-dispersive X-ray spectroscopy (EDS)

Energy-dispersive X-ray spectroscopy (EDS or EDX) is an analytical technique used to identify the elemental composition of a material. The two analysis techniques are

often used together. A high-energy electron is applied to the surface of the sample, causing the electrons to interact with the atoms of the material and excite them. The migration of an electron from the inner orbit creates a vacancy that is filled by a higher-energy electron. During this transition, the energy difference between them is released as an X-ray. Each element emits X-rays at a specific energy level. The detector in the EDS instrument measures the energy of these X-rays to produce a spectrum. Each peak in the spectrum represents an element present in the sample. The height of the peaks indicates the relative abundance of the elements. The higher peaks, correspond to higher concentrations of the respective elements in the sample.

2.2.6. X-Ray Diffraction (XRD)

X-Ray Diffraction (XRD) is a technique that can be used to study the structural properties of materials. In this technique, the sample is exposed to high-energy X-rays. The sample's ordered structure causes the atoms to diffract the incoming X-rays at specific angles. Bragg's Law is applied to analyze these diffraction patterns, which result from X-ray interferences caused by the regular arrangement of atoms. By looking at the angles at which these diffractions take place, Bragg's Law gives information about the distances between atoms and the characteristics of the crystal structure.

This technique enables the understanding of the sample's crystal structure, phase composition, size, and occasionally properties such as stress or deformation. The diffraction data captured by the detectors is analyzed using a computer, which generates a graphical pattern. This pattern serves as a "fingerprint" of the sample's structural properties, providing a detailed analysis of the material. X-ray diffraction (XRD) is an important technique for determining crystal structures in the field of materials research.

2.2.7. Raman Spectroscopy

Raman spectroscopy is a useful analytical technique for understanding the molecular and chemical properties of a material. This technique is based on the principle that laser light interacts with a material and scatters when directed at it. Raman spectroscopy is particularly recommended for studying low-frequency motions such as molecular vibrations and rotations. These properties provide valuable information about the structure and chemical bonding of the material. Most of the photons in laser light are

reflected back without losing energy when they strike a material because of elastic scattering.

This phenomenon is called Rayleigh scattering, and it has no effect on the basic analytical aspect of Raman spectroscopy. In contrast, only few photons interact with the molecules of the substance to alter their energy. Throughout this process, the energy of the photons varies along with the vibrational and rotational energy levels of the molecules. These energy shifts, often referred to as Raman scattering, form the basis of Raman spectroscopy. Since the energy shifts brought about by Raman scattering are specific to certain vibrational modes of molecules, this technique is highly useful for characterizing a substance's molecular structure and chemical bonding. Changes in the frequency of the Raman scattering light released by the material excited by the laser light are recorded by the detectors in Raman spectroscopy. The resulting spectrum can be considered a "chemical fingerprint" of the substance, revealing details about its molecular structure and chemical bonds.

Raman spectroscopy is used in many different contexts, such as materials research, biology, chemistry, and even the evaluation of artistic creations. It enables the analysis of gases, solids, liquids, and both organic and inorganic compounds. Additionally, the non-destructive nature of Raman spectroscopy makes it a particularly valuable tool. Sensitive information can be obtained, particularly at the microscopic level, and direct material study is made possible. Because of these characteristics, Raman spectroscopy is a versatile and powerful tool for the analysis of materials.

2.2.8. AFM-Based Profilometer

The AFM-based profilometer is a tool used to analyze material properties and examine fine surface details. To determine the surface's structure, this device moves an arm with a sharp tip, typically at the atomic scale, over the surface. The probe is positioned in close proximity to the surface in order to assess variations in height and surface roughness. When the apparatus is functioning, the probe moves up or down due to physical interactions between the surface's atoms as it approaches the surface. A laser beam directed at the probe precisely measures this movement. With the aid of a photodetector, the probe's movements alter the laser beam's direction, which is detected. A three-dimensional map of the surface is produced by these signals. As a result, all surface details are obtained in high resolution.

Surface roughness and height variations can be examined at the nanoscale using an AFM-based profilometer. This instrument may operate on both conductive and insulating materials and is not dependent on light, in contrast to optical profilometers. These characteristics make AFM-based profilometers a crucial analytical tool in fields such as microelectronics, nanotechnology, and materials research.

CHAPTER 3

RESULTS & DISCUSSION

3.1. Synthesis and Characterization of Molybdenum Oxide Films Using Lyotropic Liquid Crystal

First, a 2.5 mole ratio SA/C₁₂EO₁₀ Lyotropic Liquid Crystal solution was prepared. For this, 627 mg oligo (non-ionic surfactant) was added to 3 mL of ultrapure water in a glass vial and stirred with a magnetic stirrer at approximately 300 rpm until the oligo dissolved in water, and then 138 microliters of sulfuric acid added to the prepared solution to prepare a clear liquid crystal solution. Then, in a separate 25 mL falcon tube, 1.85 g of precursor chemical was used to prepare a clear solution in ultrapure water to prepare 3 mL of 0.5 M AHM solution. As a result of gradual trials, 400 microliters of 3 mL of 0.5 M AHM solution taken and added to the 2.5 mole ratio SA/C₁₂EO₁₀ Lyotropic Liquid Crystal solution prepared in a glass vial.

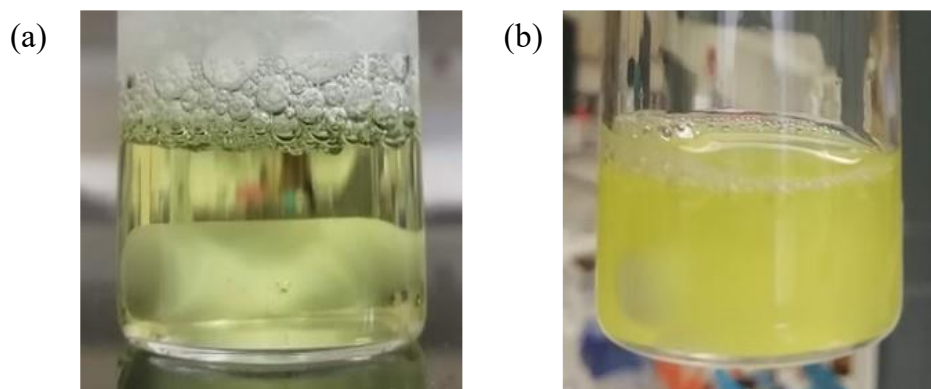


Figure 3.1 Photograph of the change of LC/AHM solution over time: (a) first minutes and (b) after 10 minutes.

The prepared AHM/LLC solution transformed from Figure 3.1 (a) to (b) in approximately 10 minutes. Therefore, the substrates to be coated were coated with a spin coater and burned within the first 10 minutes of the solution preparation. The prepared fresh solution was coated on the SiO₂ substrate surface previously cleaned with piranha solution using a spin coating device at 1000 rpm and calcined at different temperatures.

As the next step, SEM images were taken from these fired substrates. As seen in Figure 3.2 in addition to the general film image from the farthest point (300 micrometers), the image of the nanoparticles from the closest point (1 micrometer) is seen for the films calcined at (a) 250°C for 3 hours, (b) 350°C for 2 hours and (c) 450°C for 1 hour.

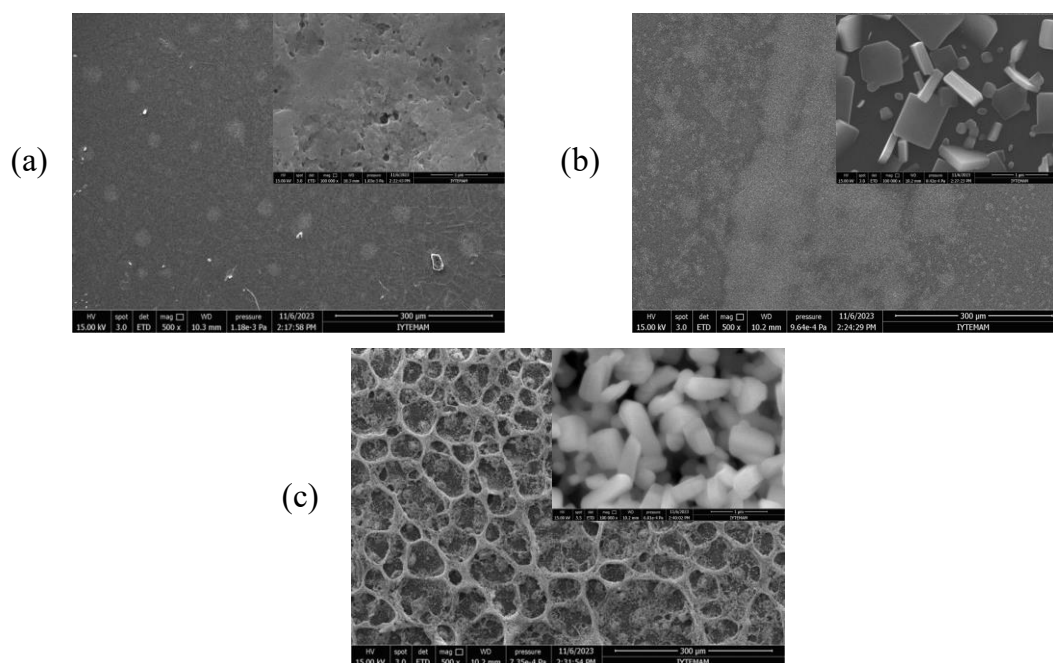


Figure 3.2. SEM images of MoO_3 films at different temperatures (a) Farthest and closest 250°C 3 hours (b) 350°C 2 hours (c) 450°C 1 hour.

When looking at SEM images, it is seen that crystallinity is low at low temperatures such as 250°C and a structure close to amorphous. As the temperature increases, crystallinity increases. When compared with SEM images in the literature,⁷¹ it is seen that crystallinity increases at high temperatures.

The EDS spectra of the MoO_3 film burned at 350°C are shown in Figure 3.3. It was obtained from the SEM image covering the entire surface of the film. It is known that each element has its own energy level. When EDS analysis is performed for MoO_3 films, each peak in the obtained spectrum indicates the presence of Mo and O elements.

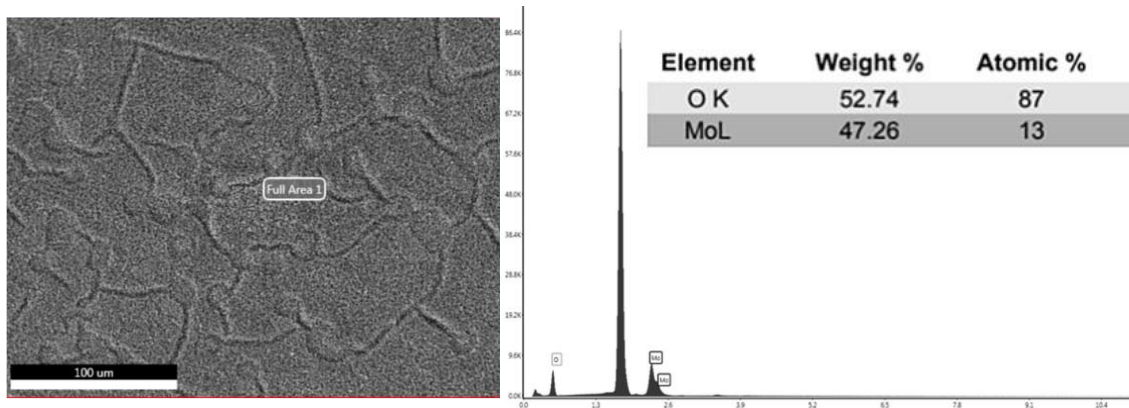


Figure 3.3. EDS image of MoO₃ film.

Diffraction angles observed in low-angle X-ray diffraction analysis of liquid crystals often provide important information for understanding the structural properties of liquid crystals. LLC mesophases exhibit a characteristic low-angle XRD pattern due to large gaps between atomic layers in the crystal lattice structure. These gaps make it difficult to maintain regular atomic arrangements and cause X-rays to diffract at certain angles. As a result, these structures exhibit low-intensity diffraction lines over a broader spectrum than conventional crystalline materials. Samples prepared from a 2.5 SA/C₁₂EO₁₀ mole ratio⁷² give a diffraction pattern at approximately 2.3°, 2θ, as shown in Figure 3.4.

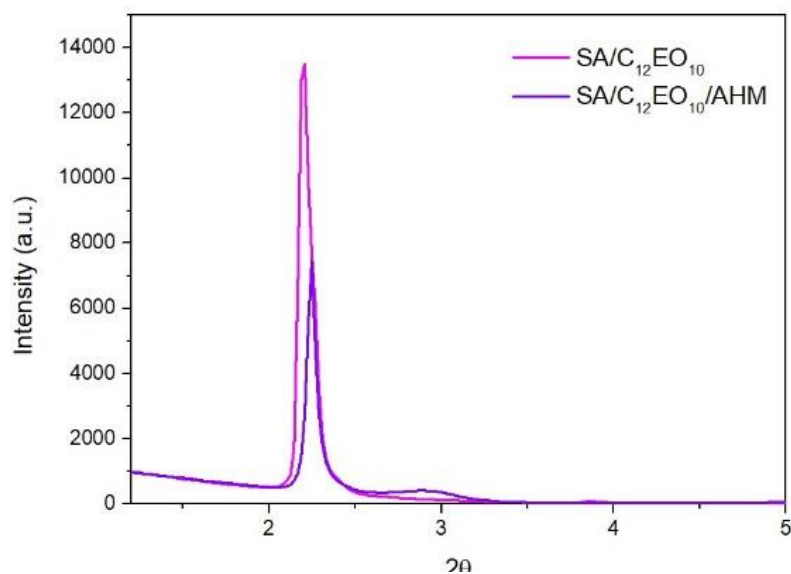


Figure 3.4. XRD pattern of SA/C₁₂EO₁₀ and SA/C₁₂EO₁₀/AHM LLC mesophases.

Depending on the thickness of the films and the measurement conditions, the intensity of the peaks may change when XRD analysis is carried out following the calcination of MoO₃ films at various temperatures (250°C, 350°C, and 450°C). Peaks with a thermodynamically stable orthorhombic a-MoO₃ crystal phase are visible in the XRD analysis result of the film that was calcined at 450 °C.

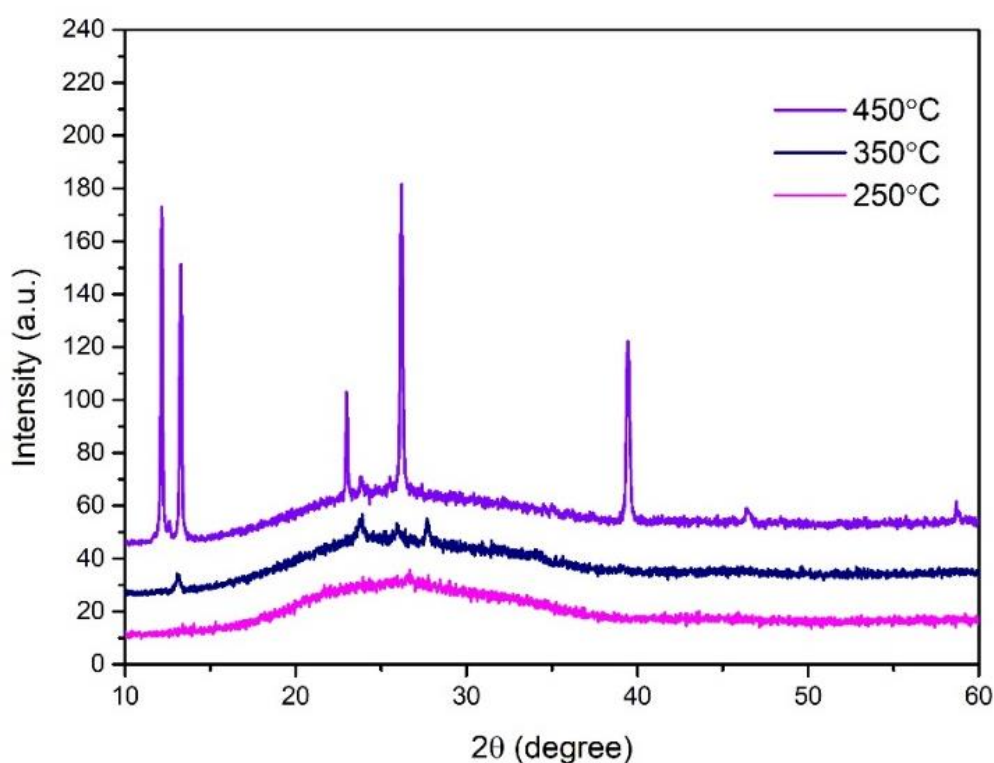


Figure 3.5. XRD pattern at different temperatures.

The XRD values of the films calcined at 350°C are seen at ~13.1°, ~23.7°, ~26°, ~27.6° and ~39.1°. According to the determined peaks, it can be said that the crystallization is not complete and a structure that is a mixture of partially crystallized and amorphous structures is formed. 250°C is generally not sufficient for the formation of the crystal phase and in this case, crystallinity is almost never formed and an amorphous structure emerges. In the literature, MoO₃ film syntheses are generally synthesized at high temperatures. As seen in Figure 3.5, since amorphous materials do not contain a regular crystal structure, no distinct peak is observed in XRD. In Figure 3.6, photographs of the transparent images of the films on the glass substrate were taken depending on the temperature. It can be said that as the temperature increases, the film

quality also increases, and the reason why the color of the film calcined at 250 degrees, which is the lowest temperature among them, is different is because the temperature is not sufficient and there is carbon left in the film.

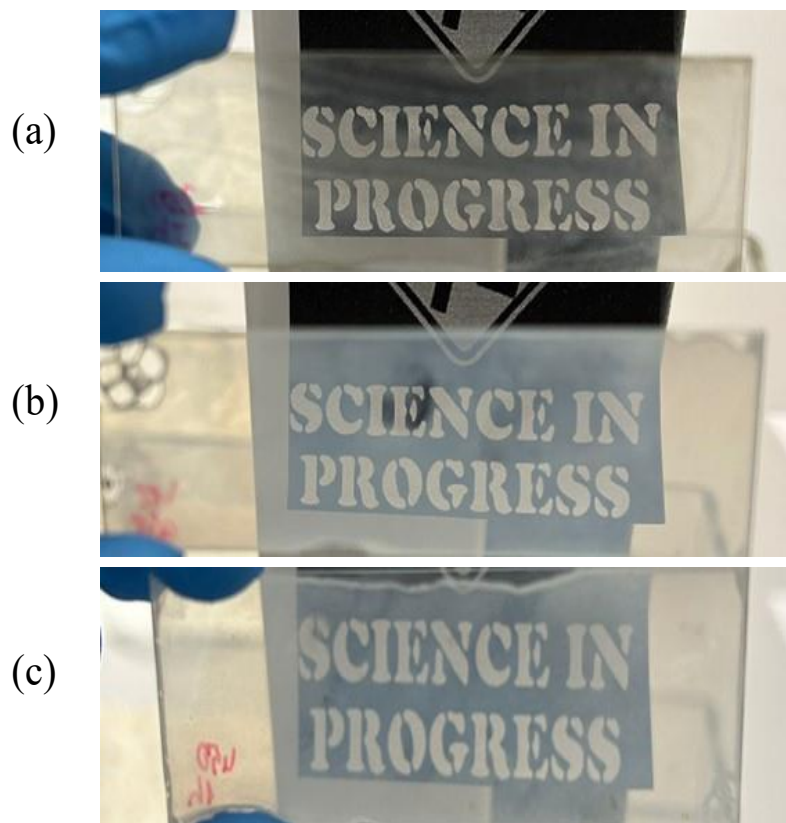


Figure 3.6. Photographs of films calcined at different temperatures on a glass slide. The temperatures are (a) 250°C, (b) 350°C, and (c) 450°C, respectively.

The peaks observed in the Raman spectrum are crucial for identifying the material's crystal structure and various crystal phases. In Figure 3.7, the Raman spectra of α -MoO₃ at various temperatures are displayed. Examination of the Raman peaks of the films calcined at 350°C and 450°C revealed distinct and sharp peaks at 994 cm^{-1} , 820 cm^{-1} , 666 cm^{-1} , 333 cm^{-1} , 282 cm^{-1} , and 158 cm^{-1} , while the films calcined at 250°C showed no peaks. The 520 cm^{-1} peak originates from the silicon substrate.

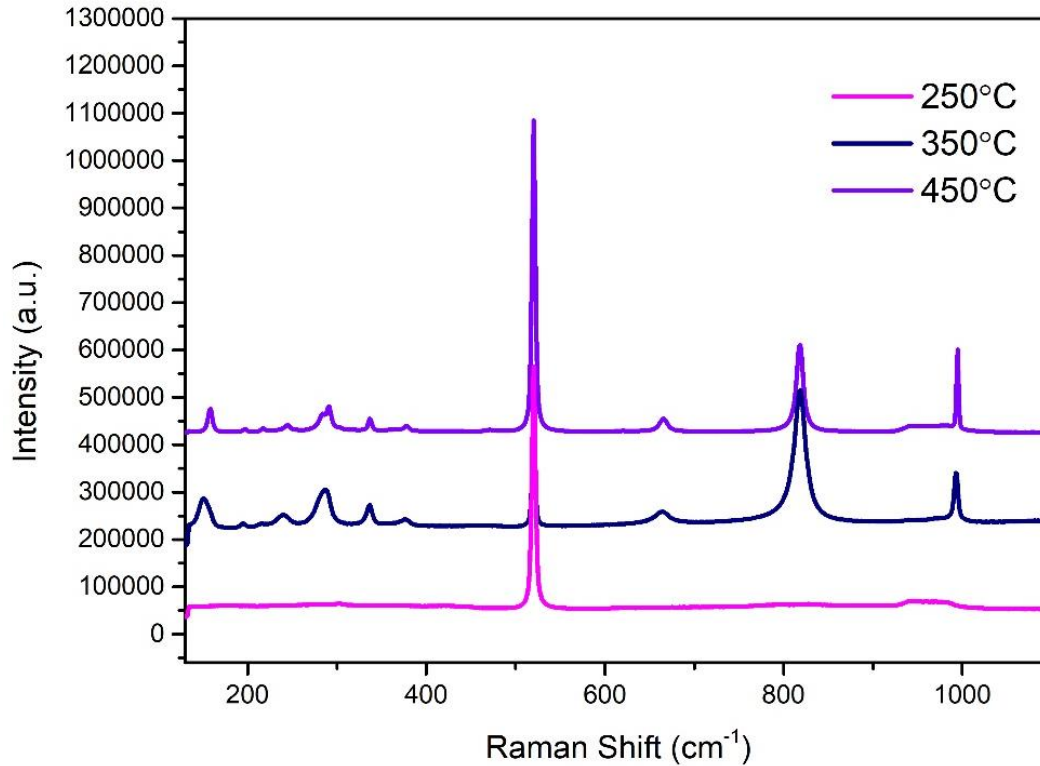


Figure 3.7. Raman Peaks of orthorhombic α -MoO₃ films prepared at different temperatures.

3.2. Synthesis and Characterization of Zinc Oxide Thin Films Using Lyotropic Liquid Crystal

Zinc Salt/C₁₂EO₁₀ LLC phases with mole ratios of 2 were used in the synthesis of liquid crystal molded zinc oxide thin films. In the synthesis, 4 mL of ethanol and 1 mL of ultrapure water were mixed in a glass vial. Then 0.500 g nonionic surfactant (10-lauryl ether, C₁₂E₁₀) was transferred to the vial and mixed homogeneously using a magnetic stirrer at 200 rpm.

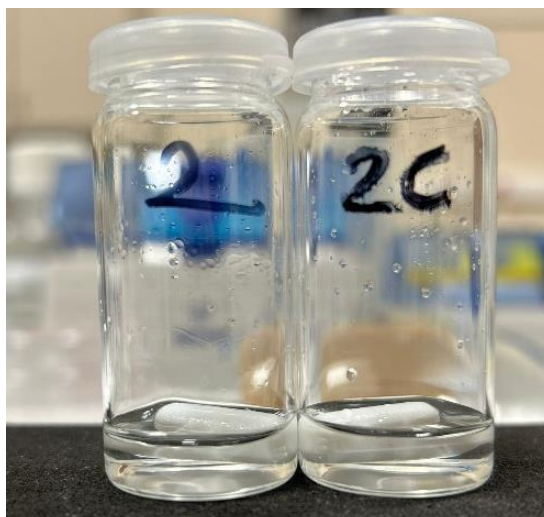


Figure 3.8. Photographs of the solutions with CTAB (2C) and without CTAB (2), both at a mole ratio of 2.

An amount of 0.442 g of zinc salt was added to the prepared LLC solutions with a 2:1 mole ratio. The solution was stirred with a magnetic stirrer at 200 rpm, resulting in transparent, clean solutions, as shown in the photograph in Figure 3.8. To investigate its effect on the film quality, a positively charged surfactant, CTAB (Cetyltrimethylammonium Bromide), was added to the system. For Zn/LLC solutions with a mole ratio of 2, 0.145 g of CTAB was added to the system at a CTAB/C₁₂EO₁₀ mole ratio of 0.5.

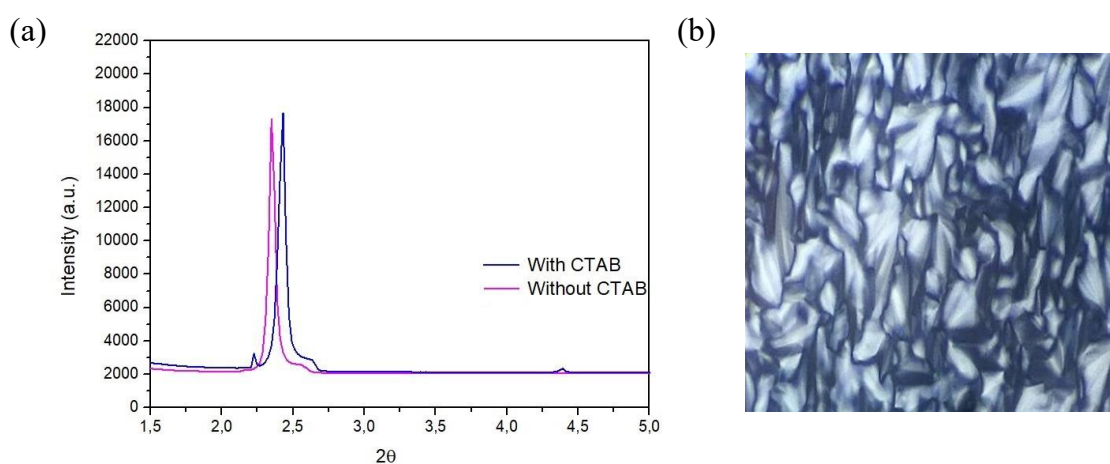


Figure 3.9. (a) Low angle XRD pattern (b) POM image of Zn/LC.

The obtained LLC solutions with and without CTAB were poured dropwise onto a glass substrate for XRD analysis and then spin-coated at 500 rpm for 2 minutes. For SEM analysis, the LLC solution was applied to the glass substrate and spin-coated at 2000 rpm for 2 minutes. Calcination was performed at 250°C for 5 hours, 350°C for 3 hours, and 450°C for 1 hour in an oxygenated environment to remove the liquid crystal and synthesize zinc oxide. In Figure 3.9(a), both the samples with and without CTAB diffract at small angles, and the images of two samples with mole ratios of 2 for these two liquid crystal solutions taken with polarized optical microscope are shown in Figure 3.9(b).

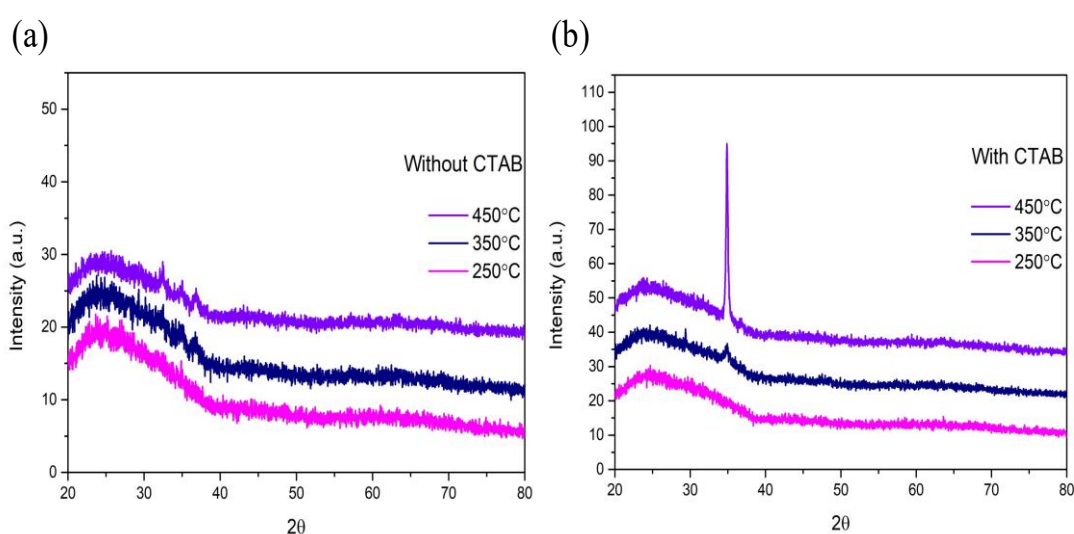


Figure 3.10. The XRD graphs of ZnO films calcined at different temperatures: (a) without CTAB, and (b) with CTAB.

The peaks observed in the XRD pattern of ZnO correspond to the characteristic planes of the wurtzite crystal structure. There are three main characteristic peaks for Zinc Oxide. These peaks are observed at approximately 31.7°, 34.4° and 36.2°. In Figure 3.10, the XRD spectra of ZnO thin films, both with and without CTAB, calcined at different temperatures are presented. The films calcined at low temperatures did not exhibit any peaks, indicating that the crystallinity of the structure is low. As the temperature increases, the crystallinity improves, leading to more prominent peaks. The ZnO thin film without CTAB (see Figure 3.10a) exhibits a polycrystalline structure, as the intensities of the three peaks between 30° and 40° are similar. In contrast, the ZnO thin film with CTAB (see Figure 3.10b) displays a prominent peak at 34.4°, which is significantly more intense than

the other peaks, indicating that the ZnO crystals are oriented perpendicular to the c-axis. In the presence of CTAB, ZnO thin films are said to be more homogeneous and have higher crystallinity.

Figure 3.11 shows SEM images of ZnO films with and without CTAB at different temperatures. It is observed that the films with CTAB at 250 °C, 350 °C, and 450 °C exhibit a more homogeneous structure compared to the films without CTAB at the same temperatures (250 °C, 350 °C, and 450 °C). CTAB, a cationic surfactant, prevents particles from aggregating, thereby promoting homogeneous film growth. As a result, it is evident that CTAB has a positive effect on the structure, particle size, and shape of the thin film.

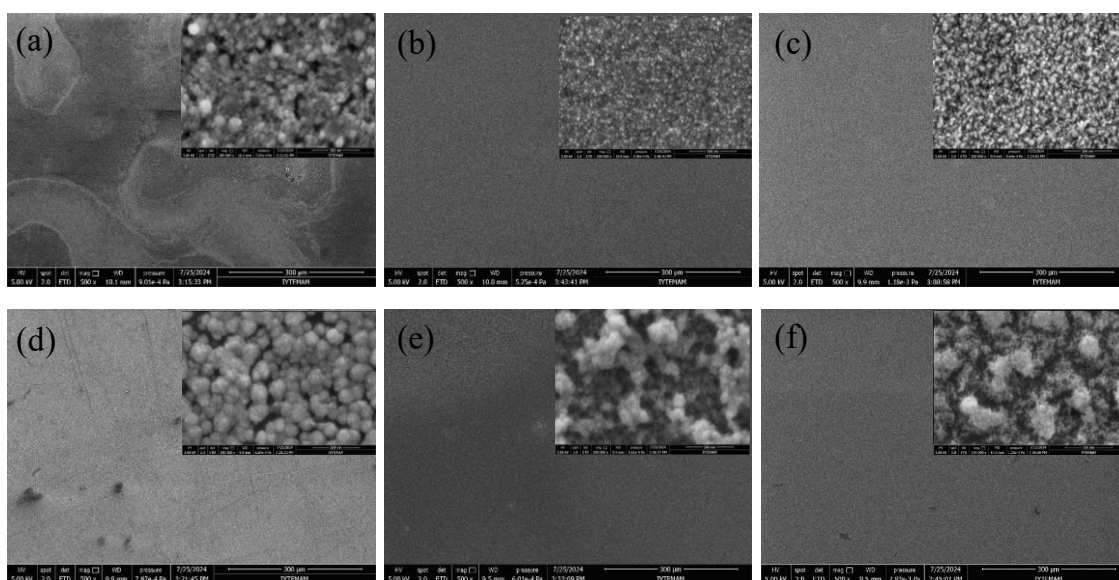


Figure 3.11. SEM images ZnO thin films at different temperatures (a) 250°C (b) 350°C (c) 450°C with CTAB and (d) 250°C (e) 350°C (f) 450°C without CTAB.

When examining the SEM images of ZnO thin films, it is observed that at lower temperatures, aggregates are formed. However, as the temperature increases, these aggregates become more homogeneous, and the crystallinity of the films improves. Additionally, it is observed that CTAB enhances the quality of the ZnO films. When examining the SEM images of the films with CTAB (see Figure 3.11a, Figure 3.11b, and Figure 3.11c), a decrease in grain size and a more homogeneous distribution are observed. In contrast, the SEM images of the films without CTAB (see Figure 3.11d, Figure 3.11e, and Figure 3.11f) reveal an increase in grain size, with the grains gathering together and

forming aggregates. As a result of the full-area EDS analysis for ZnO (see Figure 3.12), the atomic percentages of the Zn and O peaks in the spectrum (Zn: 34.57% and O: 34.27%) are very close to the 1:1 ratio, indicating that the material is pure ZnO with a wurtzite structure. Upon examining the spectrum, it is observed that elements such as Na, Mg, and Si are also present, which can be attributed to the glass substrate. A slight excess of Zn suggests the presence of oxygen vacancies in the ZnO. Peaks corresponding to elements other than zinc and oxygen originate from the glass substrate. Since the Zn and O percentages are influenced by the signals from the substrate, elemental mapping analysis was conducted specifically on the surface area containing ZnO.

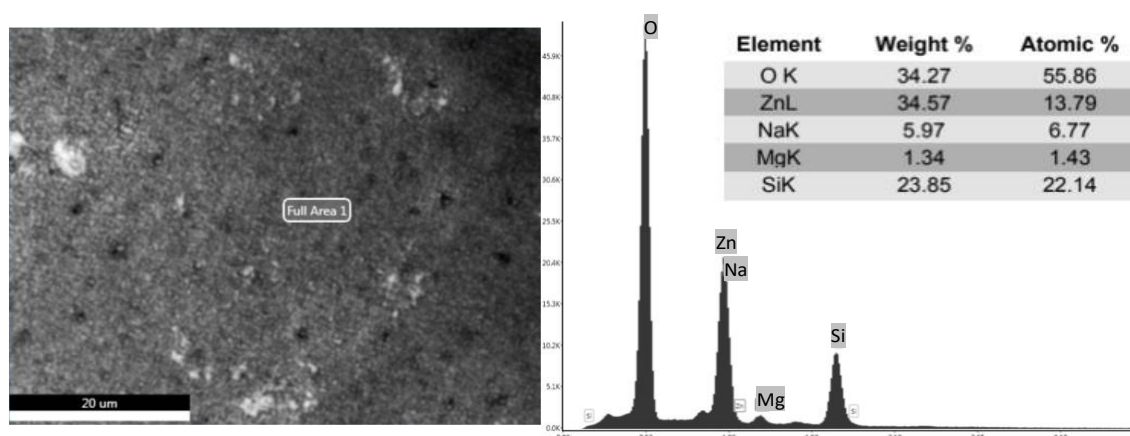


Figure 3.12. Full-area EDS analysis of the glass substrate.

EDS is highly sensitive to light elements, which may lead to an overestimation of the percentage of light elements, such as oxygen, in the analysis. This suggests that surface effects play a role. Additionally, since the glass substrate is oxygen-containing, it may have contributed to the increased oxygen percentage in the sample during EDS mapping.

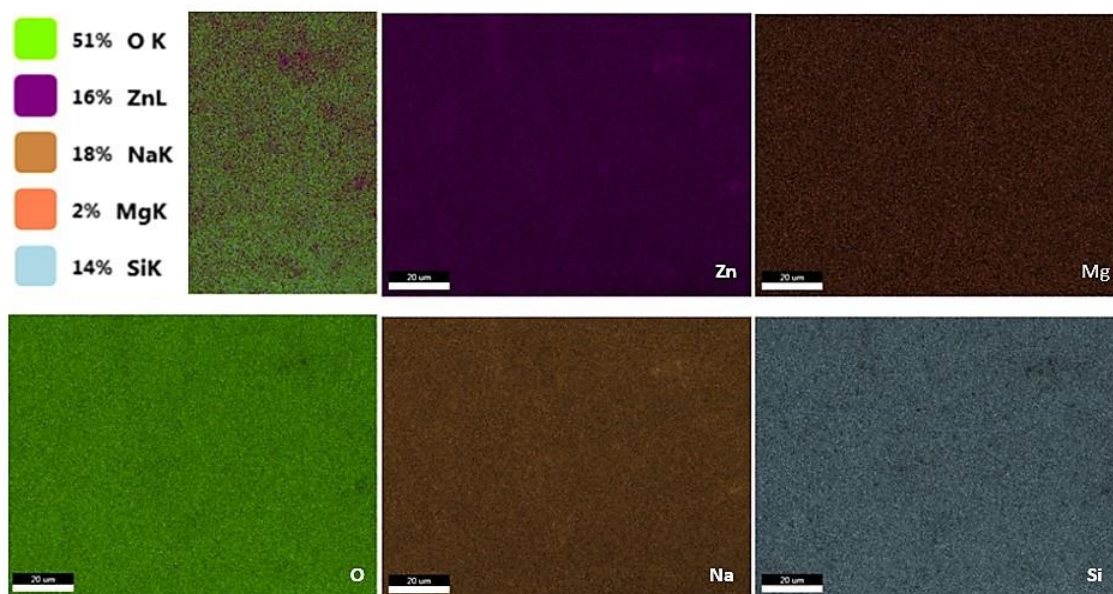


Figure 3.13. EDS mapping for ZnO thin film.

EDS is highly sensitive to light elements, which may lead to an overestimation of the percentage of light elements, such as oxygen, in the analysis. This suggests that surface effects play a role. Additionally, since the glass substrate is oxygen-containing, it may have contributed to an increased oxygen percentage in the sample during EDS mapping (see Figure 3.13).

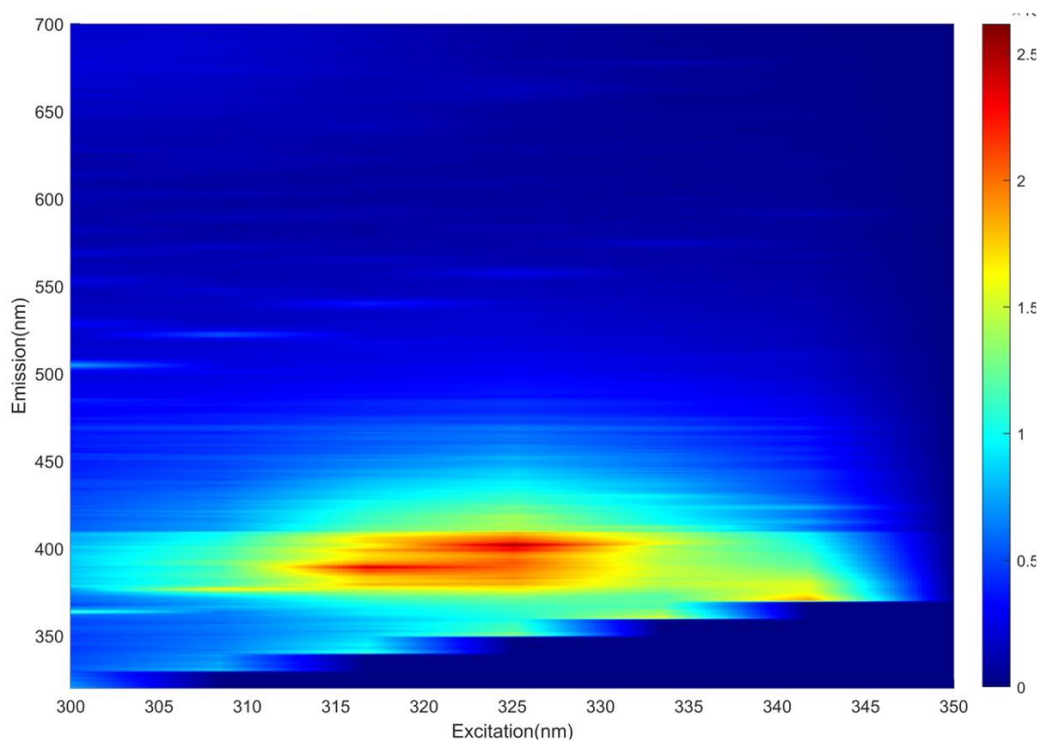


Figure 3.14. Emission mapping for ZnO Thin Film.

In the analysis of the ZnO thin film in Figure 3.14 using the FS5 device, it was determined that the film emitted at approximately 400 nm when excited at 325 nm. Excitation near the band gap of ZnO (~ 3.3 eV) causes electrons to transition into the conduction band; however, the emission at 400 nm may be attributed to intermediate energy levels created by defects, such as oxygen vacancies or excess zinc on the surface. Since this film, whose emission was measured with the FS5 device, is thicker than the other two films coated at 1000 rpm and 2000 rpm (500 rpm), zinc inhomogeneity may cause localized regions with higher zinc density.

The data obtained from the profilometer usually provides a profile of the height of the film surface. The measured height is calculated as the difference between the film and the substrate. It should be noted that the optical and electrical properties of the thin

films such as optical band gap and electrical conductivity strongly depends on the thickness of the thin film.

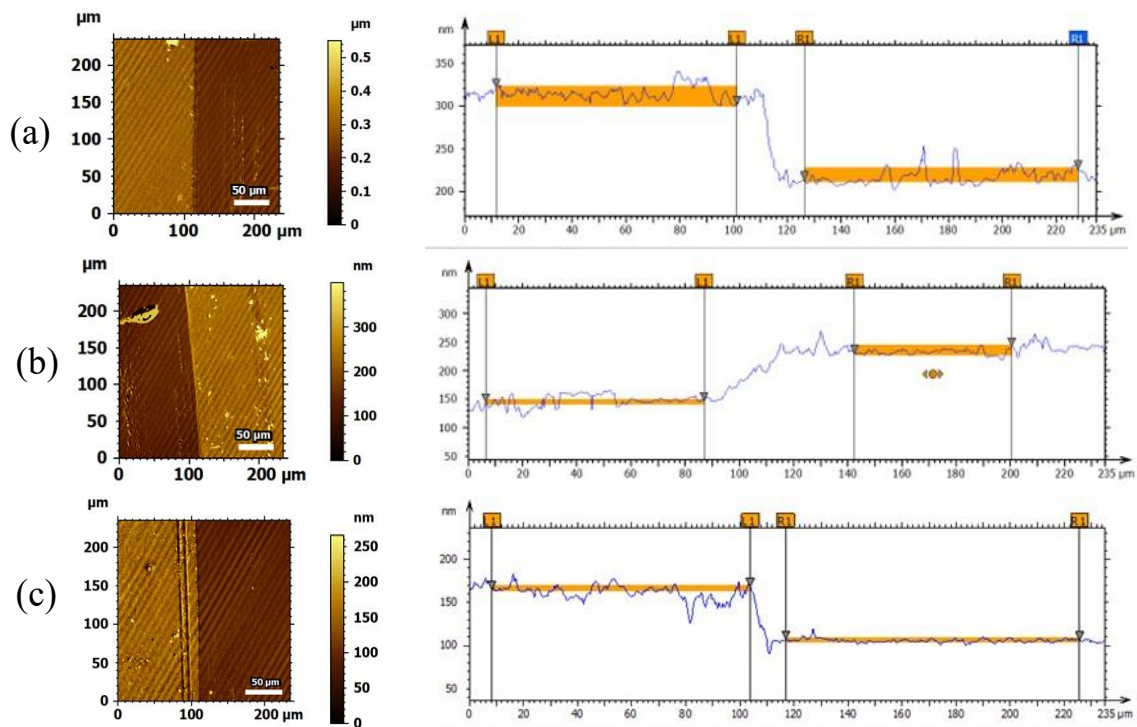


Figure 3.15. Profilometer images showing the thickness of Zinc Oxide thin films at different spin-coating speeds: (a) 500 rpm, (b) 1000 rpm, and (c) 2000 rpm.

Therefore, to calculate the band gap, the film's thickness must be known. In this study, the ZnO films with varying thicknesses had the following measurements: 99 nm for the film coated at 500 rpm, 84 nm for the film coated at 1000 rpm, and 55 nm for the film coated at 2000 rpm (see Figure 3.15).

Figure 3.16 shows the photoluminescence (PL) spectra of ZnO films produced at different spin-coating speeds (500, 1000, and 2000 rpm), highlighting how their emission properties change with film thickness. The film coated at 500 rpm has the thickest layer due to the lower coating speed. However, the graph indicates that the emission intensity of the film obtained at 500 rpm is significantly lower compared to the films coated at higher speeds

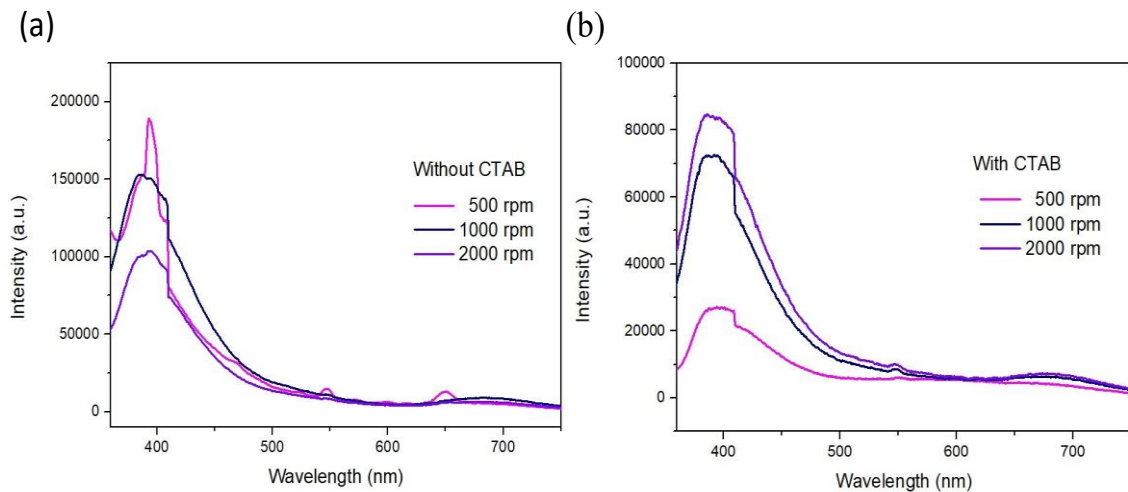


Figure 3.16. Photoluminescence (PL) spectra of ZnO films produced at different spin-coating speeds (500, 1000, and 2000 rpm): (a) without CTAB, (b) with CTAB.

Notably, the emission intensity increases as the film thickness decreases (at 1000 rpm and 2000 rpm). The highest emission intensity is observed in the thin film fabricated at 2000 rpm. Light emission is more efficient in thin films, as there is less re-absorption of light within the film. Additionally, thin films offer a more uniform surface and a more ordered crystal structure, both of which enhance optical performance and increase PL intensity.

Consequently, the emission intensity of ZnO is inversely correlated with its film thickness. While thin films produce stronger PL signals, thicker films exhibit reduced emission intensity. These findings suggest that careful control of film thickness is crucial when using ZnO films in optoelectronic applications. Moreover, CTAB doping promotes more efficient PL emission in thin films by facilitating surface modification and particle ordering.

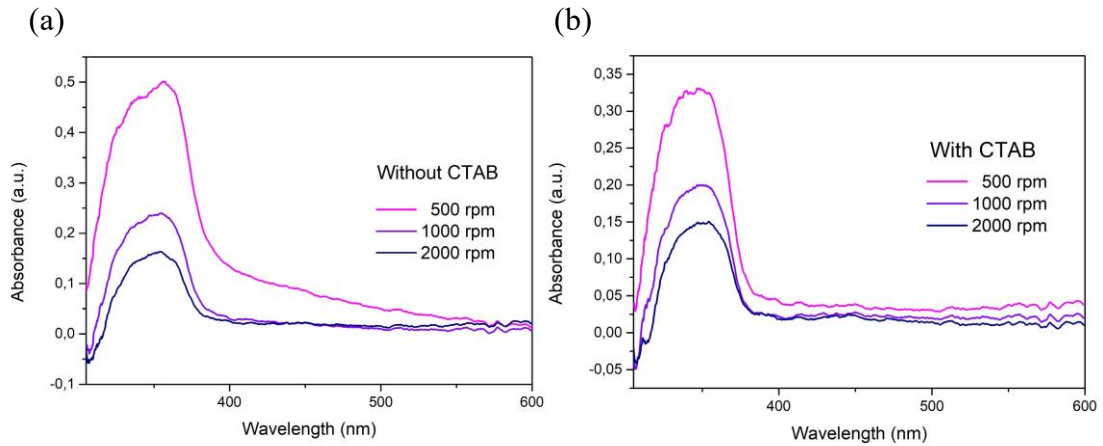


Figure 3.17. Absorbance spectra of ZnO films fabricated at different spin-coating speeds (500, 1000, and 2000 rpm): (a) without CTAB, (b) with CTAB.

In Figure 3.17(a), when CTAB is not used, the absorption is typically lower. This shows that CTAB improves the morphology of the zinc oxide film. The highest absorption is observed in the film fabricated at 500 rpm spin-coating, though it is significantly lower than that of the sample with CTAB. In the films fabricated at 1000 and 2000 rpm spin-coating, absorption decreases with increasing spin-coating speed, reflecting a reduction in light absorption capacity as the film becomes thinner. In Figure 3.17(b), the presence of CTAB significantly increased the absorption of the zinc oxide films. Especially in the films fabricated at 500 rpm spin coating, the results show that thicker films have a higher light absorption capacity. Absorption decreases as the film thickness decreases, due to the lower light absorption capacity of thinner films. This is due to the low light absorption capacity of thin films. The absorbance peak in the spectrum occurs around 360 nm, which aligns with the expected UV absorption region for zinc oxide.

Tauc Plot is a widely used method to determine the optical band gap (E_g) of a material and is usually based on absorbance (A) data. The optical band gap is calculated based on the Tauc equation: $(\alpha h\nu)^n = B(h\nu - E_g)$.⁷³ In this case, $h\nu$ represents the photon energy (eV), α the absorbance coefficient, B a constant specific to the material, and E_g the optical band gap. The type of transition determines n : for direct transitions, $n=2$, while for indirect transitions, $n=1/2$.⁷⁴

Plotting of the values of $(\alpha h\nu)n$ against $h\nu$ is done after α is determined from the absorbance data. In the resulting graph, the curve typically exhibits a linear region, which corresponds to the band gap. By extending this line to the point where it intersects the $h\nu$ axis, the optical band gap (E_g) is obtained.

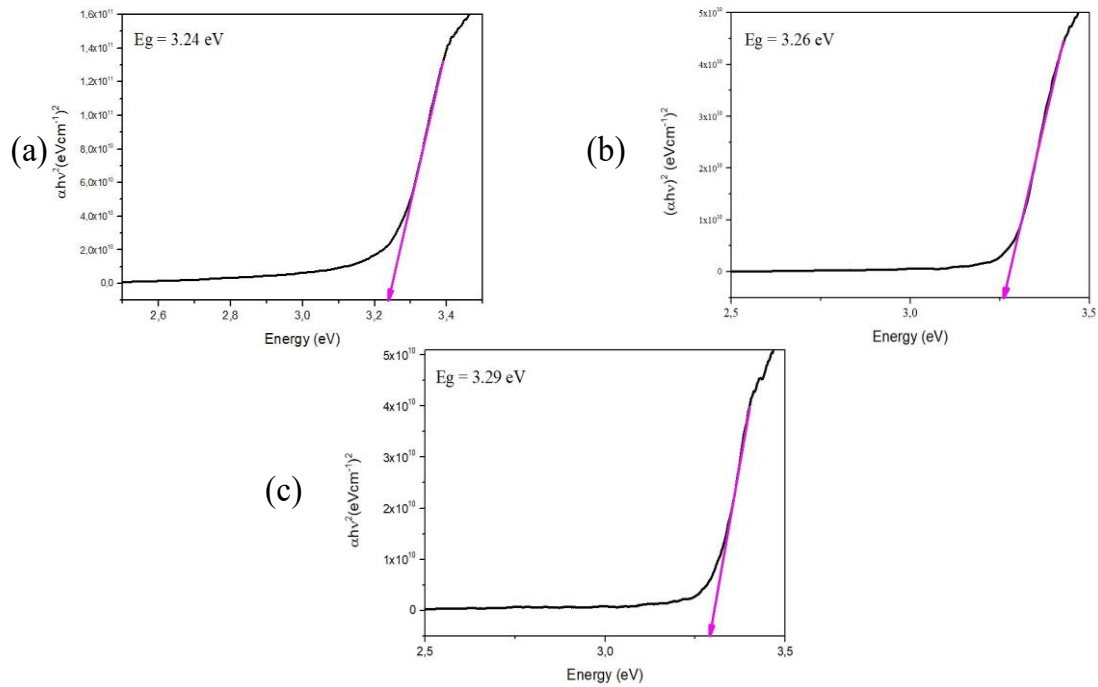


Figure 3.18. E_g determination of ZnO films different thicknesses; (a) 500 rpm, (b) 1000 rpm, (c) 2000 rpm.

The band gaps of the Zinc Oxide films, depending on their thickness, were calculated as 3.24 eV, 3.26 eV, and 3.29 eV, from the thickest film to the thinnest film. As shown in Figure 3.18. As a result of the calculations based on absorbance using the Tauc Plot method, it was observed that the band gaps increased as the film thickness decreased, i.e., from 500 rpm to 2000 rpm.

3.3. Synthesis of Liquid Crystal Templated ZIF-8 Films

In the synthesis of ZIF-8 (Zeolitic Imidazolate Framework-8) film, ZnO thin films, which had previously been coated using the spin coating method, were further coated with a 691 mM 2-methylimidazole solution. The oven was set to 30°C for three hours, 30°C for six hours, 60°C for three hours, and 60°C for six hours. After the heat treatment, the films were removed from the solution-containing vial and cleaned with water. The oven was set to 30°C for three hours, 30°C for six hours, 60°C for three hours, and 60°C for six hours. The films were removed from the solution-containing vial and cleaned with water following the heat treatment. At room temperature, the resulting ZIF-8 film was allowed to dry. On the ZnO thin film-coated glass surface, the ZIF-8 film (see Figure 3.19b) formed as a result of keeping the ZnO films (see Figure 3.19a) in a beaker with a 2-methylimidazole solution at specific temperatures, as shown in Figure 3.19.

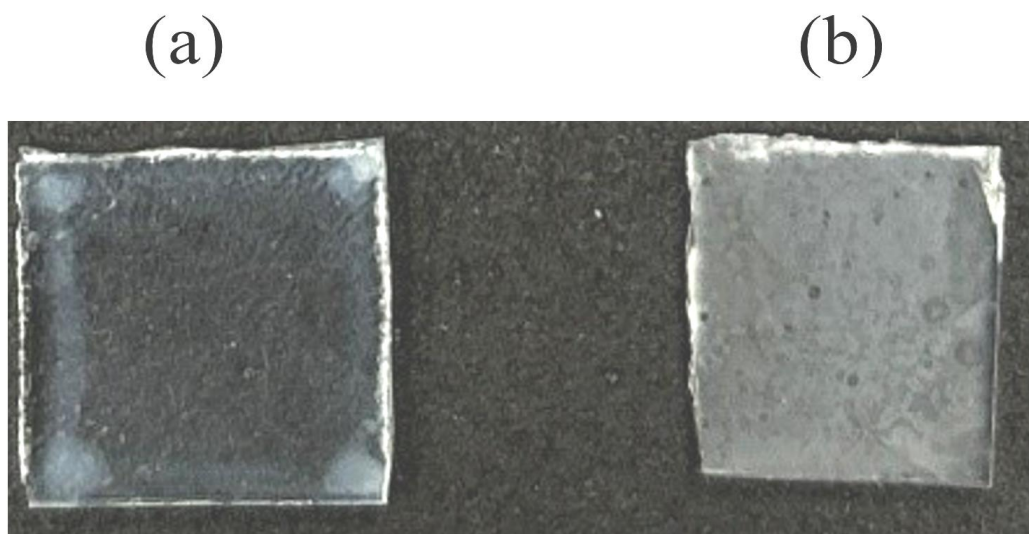


Figure 3.19. ZnO Thin Film(a) ZIF-8 Film(b)

ZIF-8 is a type of metal-organic framework (MOF) material with a highly regular crystal structure, which has been extensively studied in the literature. Compared with the literature, the peaks of the ZnO films synthesized by heating with a 2-methylimidazole solution at 30°C for 6 hours are generally located at low 2θ angles in the range of 5-20° (7.3°, 10.4°, 12.7°, 14.8°, 16.5°, 18.0°, and 24.5°). These peaks are consistent with the literature and confirm that the synthesized material has a ZIF-8 crystal structure. Shifts in the peak positions (see Figure 3.20) may indicate potential crystal defects, changes in size, or structural alterations (see Figure 3.20).

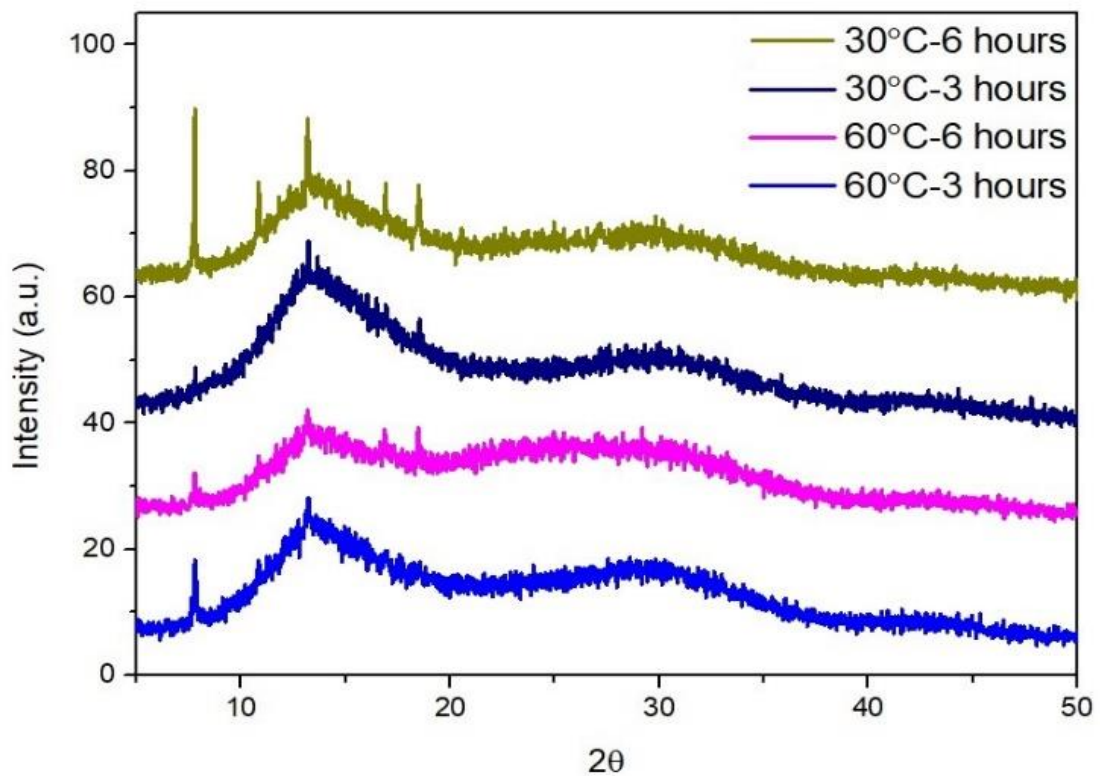


Figure 3.20. XRD graphs of ZIF-8 film structures synthesized by applying different temperature/time parameters.

Temperature and time dependent SEM images show that ZIF-8 crystals gradually appeared at the same time as the dissolution of ZnO. In Figure 3.21, the transformation times from ZnO film to ZIF-8 film are shown as follows: (a) 30°C for 3 hours, (b) 30°C for 6 hours, (c) 60°C for 3 hours, and (d) 60°C for 6 hours. As the temperature increased from 30°C to 60°C, the inter crystalline spaces were gradually filled and as a result of the continued nucleation, the ZIF-8 film was formed. Although there is no obvious cubic ZIF-8 formation at the low temperature of 30°C, the initial stages of crystallization are observed. As the temperature and time increase, the formation of ZIF-8 cubic structures also increases, leading to a gradual enhancement in crystallization.

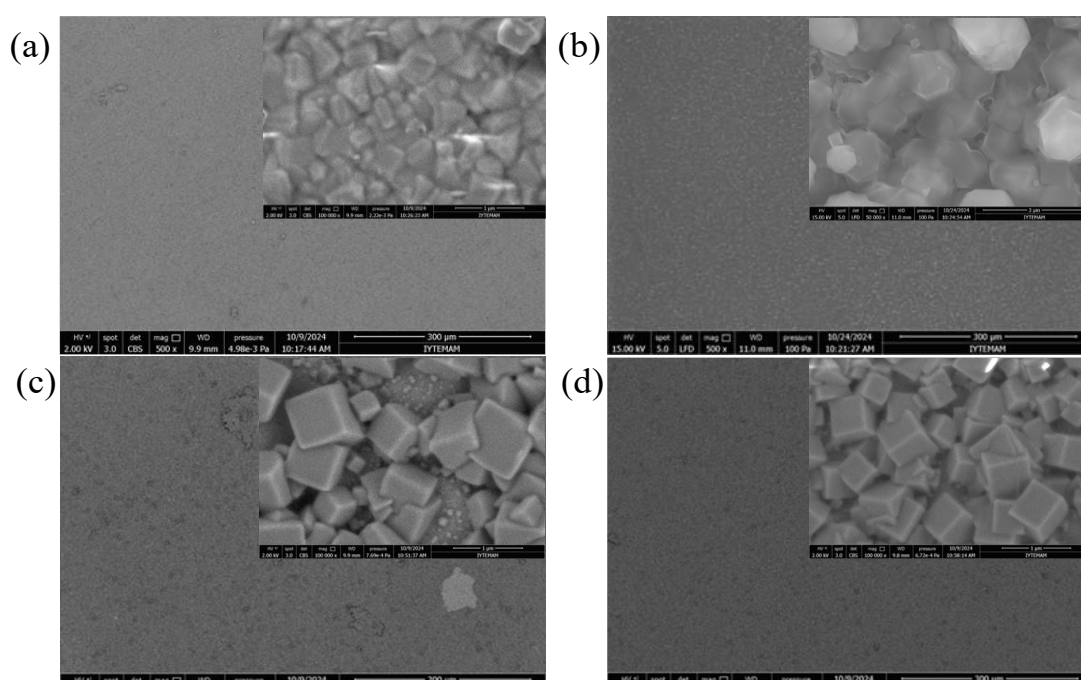


Figure 3.21. SEM images of ZIF-8 film structures formed from Zinc Oxide thin films by applying different temperature/time parameters: (a) 30°C 3 hours, (b) 30°C 6 hours, (c) 60°C 3 hours and (d) 60°C 6 hours.

CHAPTER 4

CONCLUSION

In conclusion, this thesis demonstrates that lyotropic liquid crystals (LLCs) can be used as templates in the synthesis of metal oxides, owing to their regular molecular structures and distinct phase behaviors. The importance of temperature, solvents, and additives was emphasized in the synthesis of liquid crystals. By adding metal precursor salts to the liquid crystal solution, the metal salts that accumulate around the liquid crystals are converted into metal oxides through heat treatment, with different temperature parameters (250°C, 350°C, and 450°C) being tested. As the temperature increased during the heat treatment, the liquid crystal template was gradually removed from the environment. In the synthesis of Molybdenum Trioxide film, a 0.5 M AHM solution was added to the 2.5 mole ratio SA/LLC solution system, and the coating was applied using a spin coater. Using various material characterization techniques, such as EDS, SEM, XRD, and Raman spectroscopy, the films calcined at different temperatures exhibited the orthorhombic α -MoO₃ phase, demonstrating thermal stability at 350°C and 450°C. No diffraction peaks were observed in the films heated at 250°C. This can be attributed to the material still exhibiting amorphous properties at lower temperatures. In fact, liquid crystal-templated α -MoO₃ films have a wide range of applications, including electrochromic devices and energy storage systems.

Subsequently, Zinc Oxide thin films were synthesized using liquid crystal molding. An acid-free system was used for the synthesis of Zinc Oxide films. In addition to the nonionic surfactant (10-lauryl ether) used in the liquid crystal solution, cationic CTAB was also incorporated into the system. In the high-angle XRD spectrum, it was observed that CTAB enhanced the crystallinity of the films. In addition, the SEM images revealed that the films in the CTAB system were more homogeneous, with minimal aggregation. When examining the low-angle XRD spectrum of the Liquid Crystal system with and without CTAB in the 1 to 5 degree angle range, it is observed that the liquid crystal mesophase is formed. Concurrently, it is also observed that the mesophase forms a fun-texture under the polarized optical microscope

When examining the high-angle XRD spectra with and without CTAB, it is observed that the crystallinity of the films with CTAB increases when annealed at high temperatures. However, at low temperatures, the films remain amorphous, as indicated by the absence of diffraction peaks.

Since the Oxygen and Zinc percentages are similar in the EDS analysis, pure ZnO film was synthesized. Other peaks observed in the spectrum originate from the glass substrate. When EDS mapping is performed, it is observed that the entire film surface is covered with zinc and oxygen elements. When the ZnO film was excited at 325 nm, emission was observed in the range of approximately 380 nm to 410 nm. It should be noted that since ZnO is a semiconductor with a wide band gap, when excited at 325 nm, the excited electrons quickly recombine with holes in the valence band, emitting energy close to the band gap. This energy corresponds to photons with a wavelength of approximately 400 nm. After investigating the effect of CTAB and different temperatures on ZnO thin films, the thickness of the films was measured at various stages. It was found that the thickest film (at 500 rpm) had a thickness of 99 nm, the medium thickness film (at 1000 rpm) was 84 nm, and the thinnest film (at 2000 rpm) was 55 nm, in films coated using the spin coating method with different parameters. As a result, the emission intensity of ZnO was found to be inversely proportional to the film thickness. Thin films exhibit a more regular crystal structure and surface homogeneity, which enhances their optical performance. The opposite is true for thicker films. CTAB doping enhances PL emission efficiency in thin films by promoting surface modification and improving particle arrangement.

In the absorbance spectra of ZnO films, the absorption is generally lower when CTAB is not used. The highest absorption is seen at 500 rpm, but it is significantly lower when compared to the sample with CTAB. It is seen that the light absorption capacity decreases as the film becomes thinner. The presence of CTAB caused a significant decrease in the absorption of zinc oxide films. This difference in light absorption capacity is especially noticeable in the thick films fabricated using spin-coating at 500 rpm. The absorption decreases as the film becomes thinner. This is due to the low light absorption capacity of thin films. The peak of the spectrum is around 360 nm, which coincides with the expected UV absorption region for zinc oxide. The band gaps of the films with known thicknesses were calculated using the Tauc Plot and absorbance data. It was found that the band gap was 3.24 eV for the thickest film (fabricated using spin-coating at 500 rpm),

3.26 eV for the medium thickness film (fabricated using spin-coating at 1000 rpm), and 3.29 eV for the thinnest film (fabricated using spin-coating at 2000 rpm).

Finally, solution-based ZIF-8 films were obtained from ZnO thin films. The previously synthesized ZnO films were heated in a 691 mM 2-methylimidazole solution at different temperatures and durations to form ZIF-8 films as a result of the reaction between zinc on the ZnO surface and the organic binder. The ZIF-8 films obtained were characterized using XRD measurements.

REFERENCES

1. Yu, Haifeng. *Dancing with Light: Advances in Photofunctional Liquid-Crystalline Materials*; Pan Stanford Publishing, **2015**.
2. Dunmur, D. Liquid Crystal Chemistry and Poetry. *Found Chem* **2021**, 23 (2), 277–287. <https://doi.org/10.1007/s10698-020-09394-0>.
3. DiLisi, G. A. History. In *An Introduction to Liquid Crystals*; Morgan & Claypool Publishers, **2019**; Vol. DiLisi G, 2019, pp 1-1-1–4. <https://doi.org/10.1088/2053-2571/ab2a6fch1>.
4. Garidel, P.; Kaconis, Y.; Heinbockel, L.; Wulf, M.; Gerber, S.; Munk, A.; Vill, V.; Brandenburg, K. *Send Orders for Reprints to Reprints@benthamscience.Ae Self-Organisation, Thermotropic and Lyotropic Properties of Glycolipids Related to Their Biological Implications*.
5. Kölbel, M.; Beyersdorff, T.; Tschierske, C.; Diele, S.; Kain, J. Thermotropic and Lyotropic Liquid Crystalline Phases of Rigid Aromatic Amphiphiles. *Chemistry - A European Journal* **2000**, 6 (20), 3821–3837. [https://doi.org/10.1002/1521-3765\(20001016\)6:20<382::AID-CHEM3821>3.0.CO;2-8](https://doi.org/10.1002/1521-3765(20001016)6:20<382::AID-CHEM3821>3.0.CO;2-8).
6. Dierking, I.; Al-Zangana, S. Lyotropic Liquid Crystal Phases from Anisotropic Nanomaterials. *Nanomaterials*. MDPI AG October 1, **2017**. <https://doi.org/10.3390/nano7100305>.
7. Goodby, J. W.; Görtz, V.; Cowling, S. J.; Mackenzie, G.; Martin, P.; Plusquellec, D.; Benvegnu, T.; Boullanger, P.; Lafont, D.; Queneau, Y.; Chambert, S.; Fitremann, J. Thermotropic Liquid Crystalline Glycolipids. *Chem Soc Rev* **2007**, 36 (12), 1971–2032. <https://doi.org/10.1039/b708458g>.
8. Paleos, C. M.; Tsiourvas, D. Thermotropic Liquid Crystals Formed by Intermolecular Hydrogen Bonding Interactions. *Angewandte Chemie International Edition in English*. September 1, **1995**, pp 1696–1711. <https://doi.org/10.1002/anie.199516961>.
9. Choudhury, P. K.; -Baset, A.; Ibrahim, M. A. *Introductory Chapter: Liquid Crystals and Applications*; 200AD. www.intechopen.com.
10. Rahman Rabbi, A.; Al Faysal, J. Preparation, Characterization and Applications of Liquid Crystals: A Review. *IOSR Journal of Applied Chemistry (IOSR-JAC)* **2020**, 13, 43–54. <https://doi.org/10.9790/5736-1312014354>.
11. Gridyakina, A.; Bordyuh, H.; Len, T.; Polishchuk, A. Nonlinear Optical Properties of Ionic Thermotropic and Lyotropic Liquid Crystals. *Electronics and Control Systems* **2024**, 2 (80), 67–73. <https://doi.org/10.18372/1990-5548.80.18689>.

12. Li, G. Y.; Yu, J. J.; Mo, D. M.; Bake, M.; Chen, L. F.; Li, Y. R. Electro-Optical Properties of Nematic Lyotropic Chromonic Liquid Crystals. *J Mol Liq* **2022**, *348*. <https://doi.org/10.1016/j.molliq.2021.118442>.
13. Moreno, I.; Hernández, M.; Hernández, H. *Special Section Guest Editorial Liquid Crystals for Photonics*. <https://www.spiedigitallibrary.org/terms-of-use>.
14. Tschierske, C. *Liquid Crystalline Materials with Complex Mesophase Morphologies*.
15. Albayrak, C.; Soylu, A. M.; Dag, Ö. Lyotropic Liquid-Crystalline Mesophases of [Zn(H₂O)₆](NO₃)₂-C₁₂EO₁₀-CTAB- H₂O and [Zn(H₂O)₆](NO₃)₂-C₁₂EO₁₀-SDS-H₂O Systems. *Langmuir* **2008**, *24* (19), 10592–10595. <https://doi.org/10.1021/la8022453>.
16. Çelik, Ö.; Dag, Ö. A New Lyotropic Liquid Crystalline System: Oligo(Ethylene Oxide) Surfactants with [M(H₂O)_n]_Xm Transition Metal Complexes. *Angewandte Chemie - International Edition* **2001**, *40* (20), 3800–3803. [https://doi.org/10.1002/1521-3773\(20011015\)40:20<3799::aid-anie3799>3.0.co;2-i](https://doi.org/10.1002/1521-3773(20011015)40:20<3799::aid-anie3799>3.0.co;2-i).
17. Yılmaz Topuzlu, E.; Okur, H. I.; Ulgut, B.; Dag, Ö. Role of Water in the Lyotropic Liquid Crystalline Mesophase of Lithium Salts and Non-Ionic Surfactants. *Langmuir* **2021**, *37* (49), 14443–14453. <https://doi.org/10.1021/acs.langmuir.1c02411>.
18. Ferreira, G. A. Geometric Features in Lyotropic Liquid Crystalline Phase Transitions Observed in Aqueous Surfactant Systems. *J Dispers Sci Technol* **2022**, *43* (14), 2165–2178. <https://doi.org/10.1080/01932691.2021.1924192>.
19. Dierking, I.; Al-Zangana, S. Lyotropic Liquid Crystal Phases from Anisotropic Nanomaterials. *Nanomaterials*. MDPI AG October 1, **2017**. <https://doi.org/10.3390/nano7100305>.
20. Chakraborty, T.; Chakraborty, I.; Ghosh, S. The Methods of Determination of Critical Micellar Concentrations of the Amphiphilic Systems in Aqueous Medium. *Arabian Journal of Chemistry* **2011**, *4* (3), 265–270. <https://doi.org/10.1016/j.arabjc.2010.06.045>.
21. Dierking, I.; Al-Zangana, S. Lyotropic Liquid Crystal Phases from Anisotropic Nanomaterials. *Nanomaterials*. MDPI AG October 1, **2017**. <https://doi.org/10.3390/nano7100305>.
22. Xia, Q.; Zhao, H.; Du, Z.; Zeng, Z.; Gao, C.; Zhang, Z.; Du, X.; Kulka, A.; Wierczek, K. Facile Synthesis of MoO₃/Carbon Nanobelts as High-Performance Anode Material for Lithium Ion Batteries. *Electrochim Acta* **2015**, *180*, 947–956. <https://doi.org/10.1016/j.electacta.2015.09.042>.
23. Yu, X.; Marks, T. J.; Facchetti, A. Metal Oxides for Optoelectronic Applications. *Nat Mater* **2016**, *15* (4), 383–396. <https://doi.org/10.1038/nmat4599>.

24. Bhattarai, R.; Ghimire, R. R.; Mulmi, D. Das; Thapa, R. B. Modeling of Gas Sensor Based on Zinc Oxide Thin Films by Feedback Loop Using Operational Amplifier. *Heliyon* **2024**, *10* (8). <https://doi.org/10.1016/j.heliyon.2024.e29222>.
25. Lemos, M. Z.; Jaeger, S.; Balaba, N.; Horsth, D. F. L.; Villalba, J. C.; Stefenon, F. L.; González-Borrero, P. P.; Anaissi, F. J. Synthesis and Characterization of Iron Oxides and Their Application as Inorganic Pigments in White Paint. *Coloration Technology* **2023**. <https://doi.org/10.1111/cote.12735>.
26. Yuan, S.; Duan, X.; Liu, J.; Ye, Y.; Lv, F.; Liu, T.; Wang, Q.; Zhang, X. Recent Progress on Transition Metal Oxides as Advanced Materials for Energy Conversion and Storage. *Energy Storage Materials*. Elsevier B.V. November 1, **2021**, pp 317–369. <https://doi.org/10.1016/j.ensm.2021.07.007>.
27. Grilli, M. L. Metal Oxides. *Metals*. MDPI AG June 1, **2020**, pp 1–3. <https://doi.org/10.3390/met10060820>.
28. Corby, S.; Rao, R. R.; Steier, L.; Durrant, J. R. The Kinetics of Metal Oxide Photoanodes from Charge Generation to Catalysis. *Nature Reviews Materials*. Nature Research December 1, **2021**, pp 1136–1155. <https://doi.org/10.1038/s41578-021-00343-7>.
29. An, W. J.; Thimsen, E.; Biswas, P. Aerosol-Chemical Vapor Deposition Method for Synthesis of Nanostructured Metal Oxide Thin Films with Controlled Morphology. *Journal of Physical Chemistry Letters* **2010**, *1* (1), 249–253. <https://doi.org/10.1021/jz900156d>.
30. Moumen, A.; Kumarage, G. C. W.; Comini, E. P-Type Metal Oxide Semiconductor Thin Films: Synthesis and Chemical Sensor Applications. *Sensors*. MDPI February 1, **2022**. <https://doi.org/10.3390/s22041359>.
31. Moumen, A.; Kumarage, G. C. W.; Comini, E. P-Type Metal Oxide Semiconductor Thin Films: Synthesis and Chemical Sensor Applications. *Sensors*. MDPI February 1, **2022**. <https://doi.org/10.3390/s22041359>.
32. Rebecchi, L.; Petrini, N.; Maqueira Albo, I.; Curreli, N.; Rubino, A. Transparent Conducting Metal Oxides Nanoparticles for Solution-Processed Thin Films Optoelectronics. *Optical Materials: X* **2023**, *19*. <https://doi.org/10.1016/j.omx.2023.100247>.
33. Prakash, J.; Khan, S.; Chauhan, S.; Biradar, A. M. Metal Oxide-Nanoparticles and Liquid Crystal Composites: A Review of Recent Progress. *Journal of Molecular Liquids*. Elsevier B.V. January 1, **2020**. <https://doi.org/10.1016/j.molliq.2019.112052>.
34. Luo, H.; Zhang, J.; Yan, Y. Electrochemical Deposition of Mesoporous Crystalline Oxide Semiconductor Films from Lyotropic Liquid Crystalline Phases. *Chemistry of Materials* **2003**, *15* (20), 3769–3773. <https://doi.org/10.1021/cm0345218>.

35. Zhang, W.; Chen, S. H.; Hilfiker, J. N.; Anthamatten, M. Mesomorphic Ceramic Films Synthesized via Lyotropic Self-Assembly of Metal Oxide Nanorods Complete with Sintering. *ACS Appl Nano Mater* **2020**, *3* (11), 10605–10611. <https://doi.org/10.1021/acsanm.0c01668>.
36. Serrà, A.; Vallés, E. Microemulsion-Based One-Step Electrochemical Fabrication of Mesoporous Catalysts. *Catalysts*. MDPI September 14, **2018**. <https://doi.org/10.3390/catal8090395>.
37. Zhang, X.; Shan, C.; Ma, S.; Zhao, S.; Yang, J. Synthesis of Nano-ZnS by Lyotropic Liquid Crystal Template Method for Enhanced Photodegradation of Methylene Blue. *Inorg Chem Commun* **2022**, *135*. <https://doi.org/10.1016/j.inoche.2021.109089>.
38. Shukla, R. K.; Raina, K. K. Effect of Viscosity, PH and Physicochemical Parameters of Solvent on the Aggregation and Dielectric Behaviour of Lyotropic Liquid Crystals Binary Mixtures. *J Mol Liq* **2018**, *250*, 71–79. <https://doi.org/10.1016/J.MOLLIQ.2017.11.164>.
39. Lee, C. T.; Han, S.; Zhao, Y. X.; Hung, Y. C.; Hsu, T. H.; Hsieh, H. Y.; Weng, K. W. Synthesis and Electrochromic Properties of Molybdenum Oxide Films. *Surf Coat Technol* **2019**, *363*, 426–429. <https://doi.org/10.1016/j.surfcoat.2018.12.028>.
40. Morales-Luna, M.; Arvizu, M. A.; Pérez-González, M.; Tomás, S. A. Effect of a CdSe Layer on the Thermo- A Nd Photochromic Properties of MoO₃ Thin Films Deposited by Physical Vapor Deposition. *Journal of Physical Chemistry C* **2019**, *123* (28), 17083–17091. <https://doi.org/10.1021/acs.jpcc.9b02895>.
41. Qin, P.; Zhang, S. Q.; Yung, K. K. L.; Huang, Z. F.; Gao, B. Disclosure of Charge Storage Mechanisms in Molybdenum Oxide Nanobelts with Enhanced Supercapacitive Performance Induced by Oxygen Deficiency. *Rare Metals* **2021**, *40* (9), 2447–2454. <https://doi.org/10.1007/s12598-021-01722-3>.
42. Dhanasankar, M.; Purushothaman, K. K.; Muralidharan, G. Effect of Temperature of Annealing on Optical, Structural and Electrochromic Properties of Sol-Gel Dip Coated Molybdenum Oxide Films. *Appl Surf Sci* **2011**, *257* (6), 2074–2079. <https://doi.org/10.1016/j.apsusc.2010.09.052>.
43. Chithambararaj, A.; Bose, A. C. Hydrothermal Synthesis of Hexagonal and Orthorhombic MoO₃ Nanoparticles. *J Alloys Compd* **2011**, *509* (31), 8105–8110. <https://doi.org/10.1016/j.jallcom.2011.05.067>.
44. Nsude, K. U.; Nsude, H. E.; Nwanya, A. C.; Alshoaibi, A.; Ekwealor, A. B. C.; Ezema, F. I. Molybdenum Trioxide for Supercapacitor Application: Defining the Role of Temperature and Electrolyte. *Journal of Materials Science: Materials in Electronics* **2024**, *35* (20). <https://doi.org/10.1007/s10854-024-13029-x>.

45. Wree, J. L.; Rogalla, D.; Ostendorf, A.; Schierbaum, K. D.; Devi, A. Plasma-Enhanced Atomic Layer Deposition of Molybdenum Oxide Thin Films at Low Temperatures for Hydrogen Gas Sensing. *ACS Appl Mater Interfaces* **2022**. <https://doi.org/10.1021/acsami.2c19827>.
46. Borah, D. J.; Mostako, A. T. T.; Saikia, P. K.; Dutta, P. Effect of Thickness and Post Deposition Annealing Temperature on the Structural and Optical Properties of Thermally Evaporated Molybdenum Oxide Films. *Mater Sci Semicond Process* **2019**, *93*, 111–122. <https://doi.org/10.1016/j.mssp.2018.12.038>.
47. Afify, H. H.; Hassan, S. A.; Anis, B.; Abouelsayed, A. Effect of UV Light Illumination in Humid Air on the Optical and Electronic Properties of the Orthorhombic α -MoO₃ and Monoclinic β -MoO₃. *J Appl Phys* **2022**, *132* (7). <https://doi.org/10.1063/5.0095295>.
48. Deokate, R. J.; Kate, R.; Shinde, N. M.; Mane, R. S. Energy Storage Potential of Sprayed: α -MoO₃ thin Films. *New Journal of Chemistry* **2021**, *45* (2), 582–589. <https://doi.org/10.1039/d0nj03910a>.
49. Shahzad, R. F.; Rasul, S.; Mamlouk, M.; Brewis, I.; Shakoor, R. A.; Lukose, C. C.; Zia, A. W. Designing Molybdenum Trioxide and Hard Carbon Architecture for Stable Lithium-Ion Battery Anodes. *Adv Mater Interfaces* **2024**. <https://doi.org/10.1002/admi.202400258>.
50. Trzciński, K.; Zarach, Z.; Szkoda, M.; Nowak, A. P.; Berent, K.; Sawczak, M. Controlling Crystallites Orientation and Facet Exposure for Enhanced Electrochemical Properties of Polycrystalline MoO₃ Films. *Sci Rep* **2023**, *13* (1). <https://doi.org/10.1038/s41598-023-43800-9>.
51. Fjellvåg, Ø. S.; Fjellvåg, Ø. S.; Ruud, A.; Sønsteby, H. H.; Nilsen, O.; Fjellvåg, H. Crystallization, Phase Stability, and Electrochemical Performance of β -MoO₃ Thin Films. *Cryst Growth Des* **2020**, *20* (6), 3861–3866. <https://doi.org/10.1021/acs.cgd.0c00156>.
52. Sharma, D. K.; Shukla, S.; Sharma, K. K.; Kumar, V. A Review on ZnO: Fundamental Properties and Applications. In *Materials Today: Proceedings*; Elsevier Ltd, **2020**; Vol. 49, pp 3028–3035. <https://doi.org/10.1016/j.matpr.2020.10.238>.
53. Ilkhani, M.; Dejam, L. Structural and Optical Properties of ZnO and Ni:ZnO Thin Films: The Trace of Post-Annealing. *Journal of Materials Science: Materials in Electronics* **2021**, *32* (3), 3460–3474. <https://doi.org/10.1007/s10854-020-05092-x>.
54. Sha, R.; Basak, A.; Maity, P. C.; Badhulika, S. ZnO Nano-Structured Based Devices for Chemical and Optical Sensing Applications. *Sensors and Actuators Reports* **2022**, *4*. <https://doi.org/10.1016/j.snr.2022.100098>.
55. Fischer, D.; Zagorac, D.; Schön, J. C. Fundamental Insight into the Formation of the Zinc Oxide Crystal Structure. *Thin Solid Films* **2023**, *782*. <https://doi.org/10.1016/j.tsf.2023.140017>.

56. Amakali, T.; Daniel, L. S.; Uahengo, V.; Dzade, N. Y.; de Leeuw, N. H. Structural and Optical Properties of ZnO Thin Films Prepared by Molecular Precursor and Sol–Gel Methods. *Crystals (Basel)* **2020**, *10* (2). <https://doi.org/10.3390/cryst10020132>.
57. Chaitra, U.; Kekuda, D.; Mohan Rao, K. Effect of Annealing Temperature on the Evolution of Structural, Microstructural, and Optical Properties of Spin Coated ZnO Thin Films. *Ceram Int* **2017**, *43* (9), 7115–7122. <https://doi.org/10.1016/j.ceramint.2017.02.144>.
58. Bahadur, H.; Srivastava, A. K.; Sharma, R. K.; Chandra, S. Morphologies of Sol-Gel Derived Thin Films of ZnO Using Different Precursor Materials and Their Nanostructures. *Nanoscale Res Lett* **2007**, *2* (10), 469–475. <https://doi.org/10.1007/s11671-007-9089-x>.
59. Malik, G.; Mourya, S.; Jaiswal, J.; Chandra, R. Effect of Annealing Parameters on Optoelectronic Properties of Highly Ordered ZnO Thin Films. *Mater Sci Semicond Process* **2019**, *100*, 200–213. <https://doi.org/10.1016/j.mssp.2019.04.032>.
60. Lu, Y.; Li, M.; Feng, Y.; Xu, Y.; Zhou, Y.; Xu, J.; Wang, J. Tuning the Optical Properties of Transparent ZIF-8 Thin Films by Adjusting the Crystal Morphology. *Opt Mater (Amst)* **2024**, *154*. <https://doi.org/10.1016/j.optmat.2024.115714>.
61. Pu, X.; Jiang, B.; Wang, X.; Liu, W.; Dong, L.; Kang, F.; Xu, C. High-Performance Aqueous Zinc-Ion Batteries Realized by MOF Materials. *Nanomicro Lett* **2020**, *12* (1). <https://doi.org/10.1007/s40820-020-00487-1>.
62. Siva, V.; Murugan, A.; Shameem, A.; Thangarasu, S.; Bahadur, S. A. A Simple Synthesis Method of Zeolitic Imidazolate Framework-8 (ZIF-8) Nanocrystals as Superior Electrode Material for Energy Storage Systems. *J Inorg Organomet Polym Mater* **2022**, *32* (12), 4707–4714. <https://doi.org/10.1007/s10904-022-02475-x>.
63. Lee, J. H.; Kim, D.; Shin, H.; Yoo, S. J.; Kwon, H. T.; Kim, J. Zeolitic Imidazolate Framework ZIF-8 Films by ZnO to ZIF-8 Conversion and Their Usage as Seed Layers for Propylene-Selective ZIF-8 Membranes. *Journal of Industrial and Engineering Chemistry* **2019**, *72*, 374–379. <https://doi.org/10.1016/j.jiec.2018.12.039>.
64. Li, J.; You, S.; Liu, M.; Zhang, P.; Dai, Y.; Yu, Y.; Ren, N.; Zou, J. ZIF-8-Derived Carbon-Thin-Layer Protected WC/W24O68 Micro-Sized Rods with Enriched Oxygen Vacancies as Efficient Pt Co-Catalysts for Methanol Oxidation and Oxygen Reduction. *Appl Catal B* **2020**, *265*. <https://doi.org/10.1016/j.apcatb.2019.118574>.
65. Tian, F.; Cerro, A. M.; Mosier, A. M.; Wayment-Steele, H. K.; Shine, R. S.; Park, A.; Webster, E. R.; Johnson, L. E.; Johal, M. S.; Benz, L. Surface and Stability Characterization of a Nanoporous ZIF-8 Thin Film. *Journal of Physical Chemistry C* **2014**, *118* (26), 14449–14456. <https://doi.org/10.1021/jp5041053>.

66. Uno, K.; Yamasaki, Y.; Tanaka, I. Growth Mechanisms of Zinc Oxide and Zinc Sulfide Films by Mist Chemical Vapor Deposition. *Applied Physics Express* **2017**, *10* (1). <https://doi.org/10.7567/APEX.10.015502>.
67. Al-Kutubi, H.; Dikhtiarenko, A.; Zafarani, H. R.; Sudhölter, E. J. R.; Gascon, J.; Rassaei, L. Facile Formation of ZIF-8 Thin Films on ZnO Nanorods. *CrystEngComm* **2015**, *17* (29), 5360–5364. <https://doi.org/10.1039/c5ce00590f>.
68. Lu, Y.; Li, M.; Feng, Y.; Xu, Y.; Zhou, Y.; Xu, J.; Wang, J. Tuning the Optical Properties of Transparent ZIF-8 Thin Films by Adjusting the Crystal Morphology. *Opt Mater (Amst)* **2024**, *154*. <https://doi.org/10.1016/j.optmat.2024.115714>.
69. Wei, B.; Samu, S. T.; Deng, M.; Zhou, M.; Yunqing, L.; Wang, J. ZIF-8 Thin Films Synthesized via Chemical Vapor Deposition Technique and Its Application for Gas Sensing. In *2024 22nd International Conference on Optical Communications and Networks, ICOCN 2024*; Institute of Electrical and Electronics Engineers Inc., **2024**. <https://doi.org/10.1109/ICOCN63276.2024.10648310>.
70. Zhang, X.; Xu, Y.; Valenzuela, C.; Zhang, X.; Wang, L.; Feng, W.; Li, Q. Liquid Crystal-Templated Chiral Nanomaterials: From Chiral Plasmonics to Circularly Polarized Luminescence. *Light: Science and Applications*. Springer Nature December 1, **2022**. <https://doi.org/10.1038/s41377-022-00913-6>.
71. de Castro, I. A.; Datta, R. S.; Ou, J. Z.; Castellanos-Gomez, A.; Sriram, S.; Daeneke, T.; Kalantar-zadeh, K. Molybdenum Oxides – From Fundamentals to Functionality. *Advanced Materials*. Wiley-VCH Verlag October 25, **2017**. <https://doi.org/10.1002/adma.201701619>.
72. Uzundal, C. B.; Mert Balci, F.; Ulgut, B.; Dag, Ö. Lyotropic Liquid Crystalline Mesophase of Sulfuric Acid-Nonionic Surfactant Stabilizes Lead(II) Oxide in Sulfuric Acid Concentrations Relevant to Lead Acid Batteries. *ACS Omega* **2017**, *2* (7), 3785–3791. <https://doi.org/10.1021/acsomega.7b00833>.
73. Ahmad, A. A.; Alsaad, A. M.; Albiss, B. A.; Al-Akhras, M. A.; El-Nasser, H. M.; Qattan, I. A. Optical and Structural Properties of Sputter Deposited ZnO Thin Films in Relevance to Post-Annealing and Substrate Temperatures. *Thin Solid Films* **2016**, *606*, 133–142. <https://doi.org/10.1016/j.tsf.2016.03.041>.
74. Sangiorgi, N.; Aversa, L.; Tatti, R.; Verucchi, R.; Sanson, A. Spectrophotometric Method for Optical Band Gap and Electronic Transitions Determination of Semiconductor Materials. *Opt Mater (Amst)* **2017**, *64*, 18–25. <https://doi.org/10.1016/j.optmat.2016.11.014>.
75. Zhang, H.; Liu, D.; Yao, Y.; Zhang, B.; Lin, Y. S. Stability of ZIF-8 Membranes and Crystalline Powders in Water at Room Temperature. *J Memb Sci* **2015**, *485*, 103–111. <https://doi.org/10.1016/j.memsci.2015.03.023>.
76. Serrà, A.; Vallés, E. Microemulsion-Based One-Step Electrochemical Fabrication of Mesoporous Catalysts. *Catalysts*. MDPI September 14, **2018**. <https://doi.org/10.3390/catal8090395>.

77. Sarkar, A.; Ashraf, T.; Grafeneder, W.; Koch, R. Interface Structure and Composition of MoO₃/GaAs(0 0 1). *Journal of Physics Condensed Matter* **2018**, *30* (15). <https://doi.org/10.1088/1361-648X/aab391>.
78. Samadi, M.; Zirak, M.; Naseri, A.; Kheirabadi, M.; Ebrahimi, M.; Moshfegh, A. Z. Design and Tailoring of One-Dimensional ZnO Nanomaterials for Photocatalytic Degradation of Organic Dyes: A Review. *Research on Chemical Intermediates*. Springer Netherlands April 15, **2019**, pp 2197–2254. <https://doi.org/10.1007/s11164-018-03729-5>.
79. Schernikau, M.; Sablowski, J.; Gonzalez Martinez, I. G.; Unz, S.; Kaskel, S.; Mikhailova, D. Preparation and Application of Zif-8 Thin Layers. *Applied Sciences (Switzerland)* **2021**, *11* (9). <https://doi.org/10.3390/app11094041>.